# Coupled Nonparametric Shape and Moment-Based Intershape Pose Priors for Multiple Basal Ganglia Structure Segmentation

Mustafa Gökhan Uzunbaş, Octavian Soldea*, Devrim Ünay, Müjdat Çetin, *Member, IEEE*, Gözde Ünal, *Senior Member, IEEE*, Aytül Erçil, *Member, IEEE*, and Ahmet Ekin, *Member, IEEE*

***Abstract*—This paper presents a new active contour-based, statistical method for simultaneous volumetric segmentation of multiple subcortical structures in the brain. In biological tissues, such as the human brain, neighboring structures exhibit co-dependencies which can aid in segmentation, if properly analyzed and modeled. Motivated by this observation, we formulate the segmentation problem as a maximum *a posteriori* estimation problem, in which we incorporate statistical prior models on the shapes and intershape (relative) poses of the structures of interest. This provides a principled mechanism to bring high level information about the shapes and the relationships of anatomical structures into the segmentation problem. For learning the prior densities we use a nonparametric multivariate kernel density estimation framework. We combine these priors with data in a variational framework and develop an active contour-based iterative segmentation algorithm. We test our method on the problem of volumetric segmentation of basal ganglia structures in magnetic resonance images. We present a set of 2-D and 3-D experiments as well as a quantitative performance analysis. In addition, we perform a comparison to several existent segmentation methods and demonstrate the improvements provided by our approach in terms of segmentation accuracy.**

***Index Terms*—Active contours, basal ganglia, kernel density estimation, moments, magnetic resonance (MR) imagery, shape prior, volumetric segmentation.**

Manuscript received April 05, 2010; accepted June 09, 2010. Date of publication June 28, 2010; date of current version November 30, 2010. This work was supported in part by the European Commission under Grant MTKI-CT-2006-042717, Grant FP6-2004-ACC-SSA-2 (SPICE), and Grant MIRG-CT-2006-041919, and in part by a graduate fellowship from The Scientific and Technological Research Council of Turkey (TUBITAK). *Asterisk indicates corresponding author*

M. G. Uzunbaş was with the Faculty of Engineering and Natural Sciences, Sabanci University, 34956 Istanbul, Turkey. He is now with the Computer Science Department, Rutgers University, Piscataway, 08854 USA (e-mail: uzunbas@cs.rutgers.edu).

*O. Soldea is with the Faculty of Engineering and Natural Sciences, Sabanci University, 34956 Istanbul, Turkey (e-mail: octavian@sabanciuniv.edu).

M. Çetin, G. Ünal, and A. Erçil are with the Faculty of Engineering and Natural Sciences, Sabanci University, 34956 Istanbul, Turkey (e-mail: mcetin@sabanciuniv.edu; gozdeunal@sabanciuniv.edu; aytulercil@sabanciuniv.edu).

D. Ünay is with the Electrical and Electronics Engineering Department, Bahcesehir University, Ciragan Caddesi, 34353, Istanbul, Turkey (e-mail: devrim.unay@bahcesehir.edu.tr).

A. Ekin is with the Video Processing and Analysis Group, Philips Research, Europe, 5656AE Eindhoven, The Netherlands (e-mail: ahmet.ekin@philips.com).

Color versions of one or more of the figures in this paper are available online at http://ieeexplore.ieee.org.

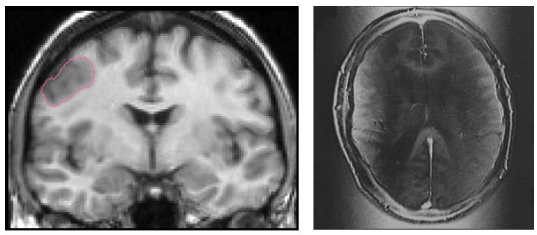

(a) (b)

Fig. 1. Artifacts in brain MR images. (a) Low-contrast, partial volume effects, courtesy of [10]. (b) Intensity inhomogeneities due to RF overflow (bias field), courtesy of [11].

## I. Introduction

MAGNETIC resonance (MR) image segmentation is fundamental in obtaining anatomical and functional information from biological structures and tissues, and it is used towards visualization, surgical guidance, quantitative analysis, and diagnosis [1]–[8]. MR image segmentation provides the location of structures of interest in a noninvasive inspection and, therefore, it is a required step when analyzing the relationships among structural and functional abnormalities, to be used for diagnosis of diseases. For example, segmentation of subcortical structures in brain MR images is motivated by a number of medical objectives including the early diagnosis of neurodegenerative illnesses such as schizophrenia, Parkinson's, and Alzheimer's diseases. In this context, the analysis of chemicals in Basal Ganglia structures is thought to provide important cues to diagnosis [9].

Segmentation of brain structures and tissues, especially in the subcortical regions, is very difficult due to limitations such as low-contrast, partial volume effects, and field inhomogeneities (see [11] and [12], and Fig. 1). In this context, most segmentation procedures still require at least some amount of manual intervention and some are performed completely manually. However, manual segmentation is tedious, time consuming, and often not reproducible. In order to compensate for these drawbacks, the scientific community has begun to develop automated clinical segmentation tools. Although many methods have been proposed for subcortical structure segmentation, such tasks still remain challenging [1], [2], [4], [5].

A significant amount of research was performed during the past three decades towards completely automated solutions for

general-purpose image segmentation. Earlier curve-propagation techniques such as snakes [13] and variational techniques [14]–[17], statistical methods [18], [19], topological atlas based methods [20], combinatorial approaches [21], and methods that perform nonparametric clustering [22] or hybrid classifiers [23] are some examples. Variational techniques provide a principled framework for formulating segmentation problems and have been widely used with biomedical data. One approach used in the solution of such problems involves active contour or curve evolution techniques.

In active contour approaches, which our framework is also based on, an initial estimate of the structure boundary is provided and various optimization methods are used to refine the initial estimate based on the input image data. Optimization of the energy functional involves the use of partial differential equations. In the definition of the energy functional, earlier methods use the boundary information for the structures of interest [13], [24], [25]. More recent methods use regional information on intensity statistics such as the mean or variance of the intensities within an area [14], [15], [26]–[29]. Due to data quality limitations, purely data-driven approaches do not usually achieve satisfactory segmentation performance. This motivates the use of prior information at various levels. In most recent active contour models, there has been increasing interest in using prior models for the shapes to be segmented. The proposed prior models can be based on distance functions, logarithm of odds-based shape representations [30], implicit shape representations, and relationships among different shapes, including pose and other geometrical relationships [31]–[39].

In this context, there are numerous automatic segmentation methods that enforce constraints on the underlying shapes. In [31], the authors introduce a mathematical formulation to constrain an implicit surface to follow global shape consistency while preserving its ability to capture local deformations. Closely related with [31], in [33] and [39], the authors employ average shapes and modes of variation through principal component analysis (PCA) in order to capture the variability of shapes. However, this technique can handle only unimodal, Gaussian-like shape densities. In [33], the image and the prior term are well separated, while a maximum *a posteriori* (MAP) criterion is used for segmentation. In [39], a region-driven statistical measure is employed towards defining the image component of the function, while the prior term involves the projection of the contour to the model space using a global transformation and a linear combination of the basic modes of variation. In [35]–[37], the authors use shape models that refer only to an average shape in an implicit form, and the prior terms refer to projections of the evolving contours via similarity transformations.

As an alternative solution to PCA limitations, [40] proposes a principal geodesic analysis (PGA) model. Another idea that has been proposed is to use kernel space shape priors [34]. As another solution to the limitation of PCA and unimodal Gaussian-like distribution models, techniques based on nonparametric shape densities learned from training shapes have been proposed in [17] and [41]. In these works, the authors assume that the training shapes are drawn from an unknown shape distribution, which is estimated by extending a Parzen density estimator to the space of shapes. The authors formulate the segmentation problem as a MAP estimation problem, in which they use a nonparametric shape prior. In particular, the authors construct the prior information in terms of a shape prior distribution such that for a given arbitrary shape one can evaluate the likelihood of observing this shape among shapes of a certain category.

The anatomical structures in the brain are related to the neighboring structures through their location, size, orientation, and shape. An integration of these relationships into the segmentation process can provide improved accuracy and robustness [42]–[45]. Recently, significant amount of work has been performed towards automatic simultaneous detection and segmentation of multiple organs. In [42], the prior probabilities of local and global spatial arrangements of multiple structures are introduced into automatic segmentation. In [46], an Expectation Maximization framework is presented in which covariant shape deformations of neighboring structures is used as prior knowledge. In [43], a joint prior based on a parametric shape model is proposed to capture covariations shared among different shape classes, which improves the performance of single object-based segmentation. With a similar approach and using a Bayesian framework, in [44] and [45] joint prior information about multiple objects is used to capture the dependencies among different shapes, where objects with clearer boundaries are used as reference objects to provide constraints in the segmentation of poorly contrasted objects. Another coupled shape prior model, which is based on the cumulative distribution function of shape features, is proposed in [47]. In that work relative interobject distances are defined as a shape feature to capture some information about the interaction between multiple objects.

Clinical applications support joint statistical shape modeling of a multiobject group rather than one of single structures outside of their multiobject context [48]. Among spatial dependencies between multiple structures, one basic aspect is intershape pose analysis [49]. Neighboring anatomical structures usually exhibit strong mutual spatial dependencies. In this context, [50] proposes a solution for the segmentation problem in the presence of a hierarchy of ordered spatial structures. In [51], the authors model the shape and pose variability of sets of multiple objects using principal geodesic analysis (PGA), which is an extension of the standard technique of principal component analysis (PCA) into the nonlinear Riemannian space.

In this paper, we take a different approach, and introduce statistical joint prior models of multistructure objects into an active contour segmentation method in a nonparametric multivariate kernel density estimation framework. We introduce prior probability densities on the coupled (joint) shapes of the structures of interest (see also [52]) Moreover, we propose a framework which includes intershape (relative) pose priors for the multistructure objects to be segmented (see also [53].)[1]

We use multivariate Parzen density estimation to estimate the unknown joint density of multistructure object shapes, as well as relative poses, based on expert-segmented training data. For intershape pose representation, we use standard moments.

[1]Pose is defined by the location, size, and orientation of an object.

Given these learned prior densities, we pose the segmentation problem as a maximum *a posteriori* estimation problem combining the prior densities with data. We derive gradient flow expressions for the resulting optimization problem, and solve the problem using active contours.

To the best of our knowledge, our approach is the first scheme of multistructure (object) segmentation employing coupled nonparametric shape and relative pose priors. As compared to existing methods [43], [45], which are based on multiobject priors, our approach takes advantage of nonparametric density estimates in order to capture nonlinear shape variability. We demonstrate the effectiveness of our approach on volumetric segmentations in real MR images accompanied by a quantitative analysis of the segmentation accuracy. We also compare our approach to existing single shape prior based approaches and demonstrate the improvements it provides in terms of segmentation accuracy.

The rest of the paper is organized as follows. In Section II, we present our coupled shape and relative pose prior-based multistructure object segmentation method. In that section, we introduce a general probabilistic framework for our active contour model, we define evolution equations, and continue with a modular description of the resulting algorithm. In Section III, we present experimental results for subcortical structures on synthetic and real MR images together with a quantitative performance analysis. We compare our method with state of the art medical image segmentation tools [42], [54]–[56], which are used in subcortical structure segmentation. In Section IV, we conclude and suggest some possible extensions and future research directions.

## II. Segmentation Based on Shape and Pose Priors

We propose a new shape and relative pose prior model embedded in an active contour framework. This model defines a new multistructure object segmentation scheme that encodes coupling among the components. In Section II-A, we introduce our probabilistic segmentation framework. In Sections II-B and II-C we provide details about the use of coupled shape priors and relative pose priors, respectively, in our segmentation framework. In Section II-D, we summarize the overall segmentation algorithm and present various implementation details.

### A. Probabilistic Segmentation Framework Based on Energy Minimization

In a typical active contour model, the segmentation process involves an iterative algorithm for minimization of an energy functional. We define our energy (cost) functional in a maximum *a posteriori* (MAP) estimation framework as

$$E(\mathbf{C}) = -\log P(\text{data}|\mathbf{C}) - \log P(\mathbf{C}) \tag{1}$$

where $\mathbf{C}$ is a set of evolving contours $\{C^1, \ldots, C^m\}$ that represent the boundaries of $m$ different anatomical structures.

In the following, we will refer to [14] as $C\&V$. We choose the likelihood term $P(\text{data}|\mathbf{C})$ as in $C\&V$. $P(\mathbf{C})$ is a coupled prior density of multi-structure objects. In this work, we focus on building $P(\mathbf{C})$.

The coupled prior is estimated using a training set of $N$ samples of the object boundaries $\{\mathbf{C}_1, \ldots, \mathbf{C}_N\}$. The essential idea of using such a prior is that the set of candidate segmenting contours $\mathbf{C}$ will be more likely if they are similar to the example shapes in the training set. The geometric information in $\mathbf{C}$ consists of the shape $\tilde{\mathbf{C}}$ and pose $\mathbf{p}$

$$P(\mathbf{C}) = P\left(\tilde{\mathbf{C}}, \mathbf{p}\right) = P\left(\tilde{\mathbf{C}}\right) \cdot P\left(\mathbf{p}|\tilde{\mathbf{C}}\right) \tag{2}$$

where $\mathbf{p}$ is a vector of pose parameters for each structure, and $\tilde{\mathbf{C}} = T[\mathbf{p}]\mathbf{C}$ denotes the aligned (or registered) version of them (i.e., $T[\mathbf{p}]$ is an alignment operator that brings the curves to a predefined reference pose, to be described in Section II-B1) below.

In this context, the coupled shape density $P(\tilde{\mathbf{C}})$ represents only joint shape variability and does not include pose variability, while $P\left(\mathbf{p}|\tilde{\mathbf{C}}\right)$ captures the joint pose variability of the structures. We decompose the pose information into global and internal (or "relative") variables

$$\mathbf{p} = (p_{glb}, \mathbf{p}_{\text{int}}) = \left(p_{glb}, p^1_{\text{int}}, \ldots, p^m_{\text{int}}\right) \tag{3}$$

where $p_{glb}$ denotes the overall (common) pose of the structures of interest and $\mathbf{p}_{\text{int}} = \left(p^1_{\text{int}}, \ldots, p^m_{\text{int}}\right)$ represents relative pose information of each structure among these $m$ structures. When the structures are globally aligned, the remaining variability in the pose of individual structures is captured by $\mathbf{p}_{\text{int}}$. Substituting (3) into (2), we have

$$P\left(\tilde{\mathbf{C}}, \mathbf{p}\right) = P\left(\tilde{\mathbf{C}}\right) \cdot P\left(p_{glb}, p^1_{\text{int}}, \ldots, p^m_{\text{int}}|\tilde{\mathbf{C}}\right). \tag{4}$$

Conditioned on $\tilde{\mathbf{C}}$, we model $p_{glb}$ and $\mathbf{p}_{\text{int}} = \left(p^1_{\text{int}}, \ldots, p^m_{\text{int}}\right)$ as independent variables

$$P\left(\tilde{\mathbf{C}}, \mathbf{p}\right) = P\left(\tilde{\mathbf{C}}\right) \cdot P\left(p_{glb}|\tilde{\mathbf{C}}\right) \cdot P\left(\mathbf{p}_{\text{int}}|\tilde{\mathbf{C}}\right). \tag{5}$$

In addition, $P(p_{glb}|\tilde{\mathbf{C}})$ is assumed to be uniform since all poses $p_{glb}$ are equally likely.[2] Then, we can express $P(\mathbf{C})$ as

$$P(\mathbf{C}) = P(\tilde{\mathbf{C}}) \cdot \gamma \cdot P\left(\mathbf{p}_{\text{int}}|\tilde{\mathbf{C}}\right) \tag{6}$$

where $\gamma$ is a normalizing scalar.

$P\left(\mathbf{p}_{\text{int}}|\tilde{\mathbf{C}}\right)$ provides a density on the relative pose of shapes. The relative pose prior is estimated over globally aligned multistructure object contours while the shape prior $P\left(\tilde{\mathbf{C}}\right)$ is estimated over both globally and locally aligned ones. Considering this key point, let $\bar{\mathbf{C}} = T[p_{glb}]\mathbf{C}$ denote the globally aligned multistructure object contours (see Fig. 2). We can then represent the relative pose prior in terms of the curves which encompass internal pose variation, conditioned on the shapes whose global and local pose variation is removed. Then the overall prior can be written as

$$P(\mathbf{C}) = P\left(\bar{\mathbf{C}}|\tilde{\mathbf{C}}\right) \cdot \gamma \cdot P\left(\tilde{\mathbf{C}}\right).$$

[2]In some applications where certain global poses are more likely *a priori*, a nonuniform density could be used.

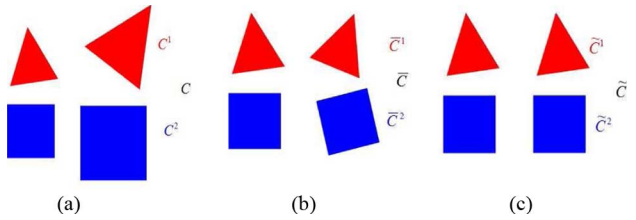


Fig. 2. Alignment terms used for a multi-object ensemble that consists of a red triangle and a blue square. In each figure, the multiobject pair on the left side is a reference for the right pair. In (a), the multiobject group $C$ (on the right) is not aligned to the left group. In (b), $\bar{C}$ is aligned globally, i.e., red and blue objects are thought as one single object and the right group is aligned to the left group. In (c), on top of $\bar{C}$, $\tilde{C}$ is aligned locally, i.e., each (sub) object on the right is aligned separately to the one on the left. In Figures (b) and (c), the multiobject ensembles are not superimposed due to illustration reasons.

Using these definitions, (1) can be expressed as

$$E(\mathbf{C}) \propto -\log P(data|\mathbf{C}) - \log P\left(\bar{\mathbf{C}}|\tilde{\mathbf{C}}\right) - \log P\left(\tilde{\mathbf{C}}\right). \tag{7}$$

Segmentation is achieved by finding the set of curves $\mathbf{C}$ that minimize (7) through active contour-based gradient flow. Given (7) above, the focus of our work is to learn and specify the priors $P\left(\bar{\mathbf{C}}|\tilde{\mathbf{C}}\right)$ and $P\left(\tilde{\mathbf{C}}\right)$. We provide the mathematical details of $P(\tilde{\mathbf{C}})$ and $P\left(\bar{\mathbf{C}}|\tilde{\mathbf{C}}\right)$ in Sections II-B and II-C below, respectively.

### B. Coupled Shape Prior for Multistructure Objects

In this section we discuss the learning and use of $P(\tilde{\mathbf{C}})$. We choose level sets as the representation of shapes [57] and we use multivariate Parzen density estimation (see [58]) to estimate the unknown joint shape distribution. We define the joint kernel density estimate of $m$ shapes as

$$P\left(\tilde{\mathbf{C}}\right) = \frac{1}{N}\sum_{i=1}^{N}\prod_{j=1}^{m} k\left(d\left(\phi_{\tilde{C}^j}, \phi_{\tilde{C}_i^j}\right), \sigma_j\right) \tag{8}$$

where $N$ is the number of training samples and $k(.,\sigma_j)$ is a Gaussian kernel with standard deviation $\sigma_j$. We use index $i$ to iterate through the training set. Similarly, we use $j$ to iterate through the structures that constitute the analyzed ensembles (for example $j$ iterates over Caudate Nucleus, Putamen, and other structures of interest). In the (8), $\phi_{\tilde{C}^j}$ is the candidate signed distance function (SDF) of the $j$th object, which is aligned to the training set, and $\phi_{\tilde{C}_i^j}$ is the SDF of the $i$th training shape of the $j$th object. Note here that, all samples in the training set are both globally and locally aligned among each other [see Fig. 2(c)]. The alignment of training samples is explained in Section II-B1 below.

Given a distance measure $d(.,.)$, the kernel for joint density estimation is constructed by multiplying separate kernels $k(.,\sigma_j)$ for each object. Our nonparametric coupled shape prior, which is defined in (8), can be used with a variety of distance metrics. Following [41], we employ the $L_2$ (Euclidean) distance $d_{L_2}$ between SDFs.

We use Gaussian kernels that operate on distances between SDFs of segmenting contours and their counterparts in the training set

$$k_i^j \triangleq k(d_{L_2}(\phi_{\tilde{C}^j}, \phi_{\tilde{C}_i^j}), \sigma_j) = \frac{\exp\left(-\frac{1}{2{\sigma_j}^2}\int_\Omega \left(\phi_{\tilde{C}^j}(\mathrm{x}) - \phi_{\tilde{C}_i^j}(\mathrm{x})\right)^2 d\mathrm{x}\right)}{\sqrt{2\pi{\sigma_j}^2}} \tag{9}$$

where x denotes the spatial domain coordinate vector. For estimation of $\sigma_j$ we refer the reader to Section III.

*1) Alignment of Training and Test Samples for Shape Prior Computations:* For learning the shape prior in (8), the pose variation of objects in the training set is removed by an alignment operation in a preprocessing step. In this operation, a set of similarity transformation parameters (translation, scaling, and rotation) is computed in order to align the training samples with each other. For alignment in 2-D problems, we use the energy-minimization based approach used in [39], and described in Appendix D-II. For alignment in 3-D, we use a faster, moment-based approach described in Appendix D-I. The $N$ training contours are aligned with one another during the training phase, i.e., $\{\mathbf{C}_1,\ldots,\mathbf{C}_N\}$ are aligned into $\left\{\tilde{\mathbf{C}}_1,\ldots,\tilde{\mathbf{C}}_N\right\}$ through a transformation $T[\mathbf{p}]$. In this procedure we fix the pose of one of the training samples and align all others to it. Fig. 2 (from a to c) represents a simple simulation of this operation for a training set of size two.

During the segmentation phase, same alignment operations are also carried out among the $j$th candidate boundary and the aligned training shapes in order to obtain $\phi_{\tilde{C}^j}(\mathrm{x})$ from $\phi_{C^j}(\mathrm{x})$ for all $j$, to be used in (8) above.

*2) Gradient Flow of the Coupled Shape Prior:* In this section, we define a gradient flow for the joint shape prior in (8). For the kernel-based density in (8) with the $L_2$ distance metric, we have

$$\frac{\partial}{\partial t}\log P\left(\tilde{\mathbf{C}}\right) = \frac{1}{N}\frac{\sum_{i=1}^{N}\left\{\sum_{j=1}^{m}\left(k_i^j\right)'\prod_{l=1,l\neq j}^{m}k_i^l\right\}}{P\left(\tilde{\mathbf{C}}\right)}. \tag{10}$$

We compute the gradient flow in the normal direction that increases most rapidly for each object contour. The gradient direction for contour $\tilde{C}^j$ is

$$\frac{\partial\phi_{\tilde{C}^j}}{\partial t} = \frac{1}{{\sigma_j}^2}\sum_{i=1}^{N}\lambda_i\left(\tilde{\mathbf{C}}\right)\left(\phi_{\tilde{C}_i^j}(\mathrm{x}) - \phi_{\tilde{C}^j}(\mathrm{x})\right) \tag{11}$$

where $j = 1\ldots m$, $\lambda_i\left(\tilde{\mathbf{C}}\right) = \prod_{j=1}^{m}k_i^j/N\cdot P\left(\tilde{\mathbf{C}}\right)$, $\sum_{i=1}^{N}\lambda_i\left(\tilde{\mathbf{C}}\right) = 1$ and x denotes the position vector. The derivation of this gradient flow can be found in Appendix B.

*3) Coupling Effect in Shape Forces:* Equation (11), defines the evolution of the contours towards shapes at the local maximum of the coupled shape prior, where $\lambda_i\left(\tilde{\mathbf{C}}\right)$ acts as the weight for the $i$th training sample. We note that training shapes that are closer to $\tilde{\mathbf{C}}$ contribute with higher weights. Furthermore, we also note that the weight function $\lambda_i\left(\tilde{\mathbf{C}}\right)$ exhibits

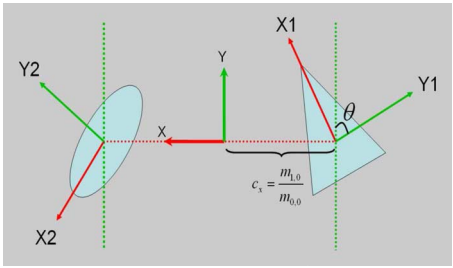


Fig. 3. Explicit representation of the relative pose parameters in a multiobject ensemble. What are illustrated as examples are the $x$ component of the relative mass center, $c_x$, as well as the angle $\theta$ of one of the objects as related to the ensemble in 2-D.

coupling between the $m$ individual structures to be segmented. In particular, this function involves a product over the kernel functions for all of the $m$ structures. This implies, for example, that a training sample (composed of curves for $m$ structures) for which the $k$th structure (where $k \in \{1 \cdots m\}$) is close to $\tilde{\mathbf{C}}_k$ will have relatively higher weights for the evolution of the other structures as well. This shows that each training sample affects the evolution as an ensemble of $m$ coupled structures rather than as $m$ independent structures.

### C. Relative Pose Prior for Multistructure Objects

In this section, we discuss the learning and use of $P(\bar{\mathbf{C}}|\tilde{\mathbf{C}})$. We estimate $P(\bar{\mathbf{C}}|\tilde{\mathbf{C}})$ through kernel density estimation as follows:

$$P(\bar{\mathbf{C}}|\tilde{\mathbf{C}}) = \frac{1}{N}\sum_{i=1}^{N}\prod_{j=1}^{m} k\left(d\left(p_{\text{int}}^{j}, p_{\text{int}}^{ji}\right), \sigma_j\right) \qquad (12)$$

where $p_{\text{int}}^{ji}$ is the relative pose of the $i$th training sample of the $j$th structure, whereas $p_{\text{int}}^{j}$ is the relative pose of the $j$th structure in the candidate (segmenting) ensemble of curves. Here $d(\cdot,\cdot)$ is a weighted Euclidean distance.[3] For estimation of $\sigma_j$ we refer the reader to Section III. We use moments to compute the relative pose parameters involved in (12). Moments provide a link between the SDF-based contour representations and the pose parameters. The relative pose $p_{\text{int}}^{ji}$ is computed over the globally aligned set of training shapes [i.e., in the $\bar{\mathbf{C}}$ space—see Fig. 2(b)]. We describe the construction of this set in Section II-C1 below. To compute the relative pose $p_{\text{int}}^{j}$ of the $j$th segmenting object, the candidate (segmenting) ensemble of curves is globally aligned to the training set, and then the relative pose $p_{\text{int}}^{j}$ is computed using moments as described in Section II-C2.

*1) Alignment of Training and Test Samples for Relative Pose Prior Computations:* In order to learn the relative poses of the structures of interest, we align the training samples globally. For each training sample (composed of multiple structure boundaries) we compute one set of similarity transformation parameters (rather than a separate set of parameters for each structure). In this way, the $N$ training contours $\{\mathbf{C}_1, \ldots, \mathbf{C}_N\}$ are aligned through the transformation $T[p_{glb}]$ to $\{\bar{\mathbf{C}}_1, \ldots, \bar{\mathbf{C}}_N\}$. Fig. 2(a) and (b) represents a simple simulation of this operation for a training set of size two. We realize this particular alignment operation using a moment-based representation of pose [59]. For the details of the algorithm we refer the reader to Appendix D-I.

During the segmentation phase, such alignment operations are also carried out among the candidate boundary and the aligned training shapes in order to obtain $\bar{C}^j$ from $C^j$, and then compute $p_{\text{int}}^{j}$ that is used in (12) above.

*2) Background on Moments and Computation of the Pose:* We now discuss the computation of the relative pose variables in (12) through moments. The relative pose of the $j$th structure is given by $p_{\text{int}}^{j} = \left[V, c_x, c_y, c_z, \bar{\Theta}\right]$. Here, $V$ is the volume, $c_x$, $c_y$, and $c_z$ are the coordinates of the structure in the $x$, $y$, and $z$ directions, respectively, and $\bar{\Theta}$ is the orientation of the structure, all computed after global alignment, as described in Section II-C1. We use moments to compute the relative poses

$$p_{\text{int}}^{j} = \left[m_{0,0,0}, \frac{m_{1,0,0}}{m_{0,0,0}}, \frac{m_{0,1,0}}{m_{0,0}}, \frac{m_{0,0,1}}{m_{0,0}}, \bar{\Theta}\right]. \qquad (13)$$

In (13) above, $m_{0,0,0}$ corresponds to volume, $m_{1,0,0}/m_{0,0,0}$, $m_{0,1,0}/m_{0,0,0}$, and $m_{0,0,1}/m_{0,0,0}$ correspond to $x$, $y$, and $z$ positions relative to the ensemble mass center, and $\bar{\Theta}$ corresponds to the canonic orientation of the $j$th structure relative to the orientation of the ensemble. In this context, we present a solution where $\bar{\Theta}$ is a vector that consists of three components, $\bar{\Theta} = [\theta_x, \theta_y, \theta_z]$, which are angles that represent the rotation of an object related to inertia axes. These angles are defined by the inertia tensor, to be defined in the following [see (16)]. Fig. 3 contains a simple sketch illustrating (some of) the relative pose parameters in a two-object ensemble in 2-D.

Following [60], the 3-D moment of order $p+q+r$, of an image function, $f(x,y)$, is defined as

$$m_{p,q,r} = \int_{x=-\infty}^{\infty}\int_{y=-\infty}^{\infty}\int_{z=-\infty}^{\infty} x^p y^q z^r f(x,y,z)\, dxdydz.$$

The 3-D moment for a $(P \times Q \times R)$ discretized image, $f(x,y,z)$, is

$$m_{p,q,r} = \sum_{x=0}^{P-1}\sum_{y=0}^{Q-1}\sum_{z=0}^{R-1} x^p y^q z^r f(x,y,z).$$

Focusing on moments of objects, we use

$$f(x,y,z) = \begin{cases} 1, & \text{if } (x,y,z) \text{ is inside the object} \\ 0, & \text{otherwise.} \end{cases}$$

We compute moments of objects that are geometric shapes and are, therefore, inherently defined by their boundaries. Using this fact, we evaluate moments of segmenting curve or surface using the heaviside function of its SDF, where heaviside is defined as

$$H(x) = \begin{cases} 1, & x \geq 0 \\ 0, & \text{otherwise} \end{cases} \qquad \delta(x) = \frac{dH}{dx}. \qquad (14)$$

The boundary of the object defines the domains of integration (or summation in the discrete case), which we denote by $\Omega$. With these notations, we compute the 3-D moment of order $p+q+r$, using the formula $m_{p,q,r} = \int_{\Omega} x^p y^q z^r f(x,y,z)\, dxdydz$. In particular, given the embedding function $\phi(x,y,z)$ of the object shape, where $\phi$ is a signed distance function, we define $f(x,y,z) = H(-\phi(x,y,z))$ and, therefore, $m_{p,q,r} = \int_{\Omega} x^p y^q z^r H(-\phi(x,y,z))\, dxdydz$.

[3]We consider weights that sum up to one.

Note that whenever $\phi(x,y,z) < 0$, the argument $(x,y,z)$ is located inside the object. Thus, $H(x)$ takes value 1 for the inside region of the object according to (14) above. In practical implementations we employ $H_\epsilon$ and $\delta_\epsilon$, which are approximations to $H$ and $\delta$, respectively, see [14].

Define $\mathcal{M}$ be the set of all moments. Let $M_0 = \{m_{0,0,0}\}$, $M_1 = \{m_{1,0,0}, m_{0,1,0}, m_{0,0,1}\}$ and $M_n = \{m_{i,j,k} | m_{i,j,k} \in \mathcal{M}, i+j+k = n\}$ for any $n \geq 0$. In addition, define the complete set of moments of order up to order two by

$$\mathcal{M}_2 = M_0 \bigcup M_1 \bigcup M_2.$$

In order to characterize the orientation of an object, we employ the inertia tensor. Following [61], define the inertia moments as

$$\begin{cases} I^{xx} = m_{0,2,0} + m_{0,0,2} - \frac{m_{0,1,0}^2}{m_{0,0,0}} - \frac{m_{0,0,1}^2}{m_{0,0,0}} \\ I^{yy} = m_{2,0,0} + m_{0,0,2} - \frac{m_{1,0,0}^2}{m_{0,0,0}} - \frac{m_{0,0,1}^2}{m_{0,0,0}} \\ I^{zz} = m_{2,0,0} + m_{0,2,0} - \frac{m_{1,0,0}^2}{m_{0,0,0}} - \frac{m_{0,1,0}^2}{m_{0,0,0}} \\ I^{xy} = I^{yx} = m_{1,1,0} - \frac{m_{1,0,0} m_{0,1,0}}{m_{0,0,0}} \\ I^{xz} = I^{zx} = m_{1,0,1} - \frac{m_{1,0,0} m_{0,0,1}}{m_{0,0,0}} \\ I^{yz} = I^{zy} = m_{0,1,1} - \frac{m_{0,1,0} m_{0,0,1}}{m_{0,0,0}}. \end{cases} \quad (15)$$

In other words, inertia moments are defined using moments of objects centered in their mass centers. Moreover, consider the following matrix:

$$\bar{I}_{3-D} = \begin{pmatrix} I^{xx} & -I^{xy} & -I^{xz} \\ -I^{yx} & I^{yy} & -I^{yz} \\ -I^{zx} & -I^{zy} & I^{zz} \end{pmatrix} \quad (16)$$

also known as the inertia tensor [61]. We analyze the products of inertia, i.e., $I^{xy}$, $I^{yx}$, $I^{xz}$, $I^{zx}$, $I^{yz}$, and $I^{zy}$ and the principal moments of inertia, i.e., $I^{xx}$, $I^{yy}$, and $I^{zz}$. We represent the orientation of an object as a three component vector $\bar{\Theta} = [\theta_x, \theta_y, \theta_z]$, where $\theta_x$, $\theta_y$, and $\theta_z$ are rotation angles around $Ox$, $Oy$, and $Oz$ axes, respectively. This decomposition employs Euler angles, see [62] and [63].

Next, we introduce characterizations of $\theta_x$, $\theta_y$, and $\theta_z$ in terms of moments. Consider without loss of generality $\theta_z$, which also represents the angle between the projections of the eigenvectors of $\bar{I}_{3-D}$ on $xy$ plane and the coordinate axes $Ox$ and $Oy$, (see [60], [62]). In order to evaluate $\theta_z$, we follow the Jacobi procedure in [64], where annihilation rotation matrices are used towards diagonalization of symmetric matrices. In this context, note that the inertia tensor in (16) is a symmetric matrix. Bearing in the mind that the angle

$$\theta_z = \frac{1}{2} \arctan\left(\frac{2I^{xy}}{I^{yy} - I^{xx}}\right) \quad (17)$$

depends on $\bar{\mathbf{C}}$, and substituting (15) into (17), we obtain

$$\theta_z\left(\bar{\mathbf{C}}\right) = \frac{1}{2} \arctan \times \left(\frac{2\left(m_{1,0,0}m_{0,1,0} - m_{1,1,0}m_{0,0,0}\right)}{\left(m_{0,2,0} - m_{2,0,0}\right)m_{0,0,0} + m_{1,0,0}^2 - m_{0,1,0}^2}\right). \quad (18)$$

Of course, similar expressions hold for $\theta_x$ and $\theta_y$.

Now let us discuss the use of these moment-based representations for the density estimate in (12). The Gaussian kernel functions appearing in (12) can be expressed as

$$\begin{aligned} k_i^j &\triangleq k\left(d\left(p_{\text{int}}^j, p_{\text{int}}^{ji}\right), \sigma_j\right) \\ &= \frac{1}{\sqrt{2\pi\sigma_j{}^2}} \exp\left\{ -\frac{1}{2\sigma_j{}^2}\left[ w_0^j \left(m_{0,0,0}^j - m_{0,0,0}^{ji}\right)^2 \right.\right. \\ &\quad + \sum_{m_{r,s,t} \in \mathcal{M}_2, r+s+t=1} w_{1,r,s,t}^j \left(\frac{m_{r,s,t}^j}{m_{0,0,0}^j} - \frac{m_{r,s,t}^{ji}}{m_{0,0,0}^{ji}}\right)^2 \\ &\quad + w_{2,x}^j \left(\bar{\theta}_x^j - \bar{\theta}_x^{ji}\right)^2 + w_{2,y}^j \left(\bar{\theta}_y^j - \bar{\theta}_y^{ji}\right)^2 \\ &\quad \left.\left. + w_{2,z}^j \left(\bar{\theta}_z^j - \bar{\theta}_z^{ji}\right)^2 \right] \right\} \end{aligned} \quad (19)$$

where $w_0^j$, $w_{1,r,s,t}^j$, $w_{2,x}^j$, $w_{2,y}^j$, and $w_{2,z}^j$ are weights. We consider weights that sum up to one[4]. Here, $m_{r,s,t}^j$ and $m_{r,s,t}^{ji}$ denote the moments of $\bar{C}^j$ and $\bar{C}_i^j$, respectively, and the angles $\theta$ follow the same convention.

*3) Gradient Flow of the Relative Pose Prior:* Next, we present the gradient flow for the relative pose prior in (12). The gradient flow of (12) is

$$\frac{\partial \phi_{\bar{C}^j}}{\partial t} = \frac{\sum_{i=1}^{N}\left(\prod_{l=1}^{m} k_i^l\right) \text{MPF}(j,i)}{{\sigma_j}^2 P\left(\bar{\mathbf{C}}|\tilde{\mathbf{C}}\right) \cdot N} \delta_\epsilon\left(\phi_{\bar{C}^j}\right) \quad (20)$$

$$\begin{aligned} \text{MPF}(j,i) &= w_0^j \left(m_{0,0,0}^j - {m_{0,0,0}}^{ji}\right) \\ &\quad + \sum_{m_{r,s,t}^j \in \mathcal{M}_2, r+s+t=1} w_{1,r,s,t}^j \left(\frac{m_{r,s,t}^j}{m_{0,0,0}^j} - \frac{m_{r,s,t}{}^{ji}}{{m_{0,0,0}}^{ji}}\right) \cdot \\ &\quad \frac{\left(x^r y^s z^t m_{0,0,0}^j - m_{r,s,t}^j\right)}{\left(m_{0,0,0}^j\right)^2} \\ &\quad + w_{2,x}^j \left(\bar{\theta}_x^j - \bar{\theta}_x^{ji}\right) \sum_{s=0}^{2} \sum_{t=0}^{2-s} y^s z^t M_{st}^{\theta_x j} \\ &\quad + w_{2,y}^j \left(\bar{\theta}_y^j - \bar{\theta}_y^{ji}\right) \sum_{r=0}^{2} \sum_{t=0}^{2-r} x^r z^t M_{rt}^{\theta_y j} \\ &\quad + w_{2,z}^j \left(\bar{\theta}_z^j - \bar{\theta}_z^{ji}\right) \sum_{r=0}^{2} \sum_{s=0}^{2-r} x^r y^s M_{rs}^{\theta_z j} \end{aligned} \quad (21)$$

for each $j \in \{1, \ldots, m\}$. The derivation of this gradient flow can be found in Appendix C. In (21), the short notation term $M_{a,b}^{\theta_w j}$ depends on $\theta_w$ (of the evolving shapes). For example, when $w = z$, $a$ and $b$ refer to $r$ and $s$, respectively. The complete definition and details of $M_{a,b}^{\theta_w j}$ can be found in Appendix C. Note that in (21), only $r$, $s$, and $t$ represent exponential arguments, all other superscripts are indices.

During the evolution of the level sets, the relative pose parameters $p_{\text{int}}^j$ are implicitly updated. We show the influence of

[4]In (9) and (19) we use the same kernel notation for shape and relative pose prior modeling. The distinction should be clear from context.

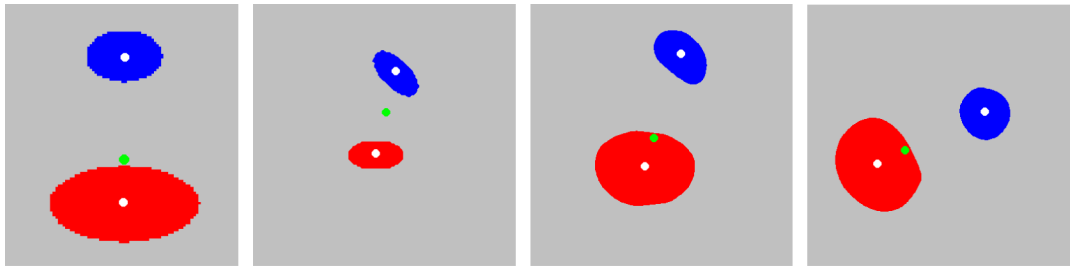

(a) (b) (c) (d)

Fig. 4. Moment-based relative pose reconstruction. The small white circles are the mass centers of the corresponding objects. The green small circles are the mass centers of the blue and red objects together. (a) Training set. (b) Initialization. (c) Iteration 140. (d) Steady state after iteration 200.

TABLE I
AREA AND MASS CENTER DISTANCE (MCD) RECONSTRUCTION MEASUREMENTS IN PIXELS FOR THE EVOLUTION EXPERIMENT ILLUSTRATED IN FIG. 4. MCD IS THE DISTANCE BETWEEN THE WHITE (CORRESPONDING) MASS CENTER AND THE GREEN ONE IN PIXELS

| | Ratios | | Relative orientation i.e. angles difference |
|---|---|---|---|
| | Areas | MCDs | |
| Training | 0.3333 | 3.0000 | 0.0000 |
| Initialization | 0.9900 | 1.0200 | 0.7900 |
| Iteration 140 | 0.3300 | 3.0500 | −0.7400 |
| Steady state | 0.3400 | 2.8300 | −0.0860 |

the relative pose prior on contour evolution in a 2-D example. This experiment demonstrates the evolution component based solely on relative pose prior information. We illustrate the moment-based evolution towards the reconstruction of the relative pose of two ellipses in Fig. 4. In this experiment, we observe an evolution driven solely by priors on relative areas, relative positions, and relative orientations of two objects. Neither priors on shape, nor any data term are used in the evolution. Furthermore, there is no global positioning information, either. Hence, we just observe a coherent deformation on the objects such that they try to resemble the training samples in terms of relative pose. For clarity, relative areas means their size ratio; relative position means the distance between the mass center of a structure and the one of the ensemble; relative orientation means the angle between the principal axes of the two objects. We present these parameters in Table I. In the training set, for simplicity, we use only one training sample in which we have two arbitrarily positioned parallel ellipses with size ratio of three and the same orientation [see Fig. 4(a)]. Therefore, the ratio of relative positions is also three. These ratios are shown in Table I. In Fig. 4, each white small circle shows the mass center of the object encircling it. The small green circle is the mass center of the ensemble. An arbitrary initialization with size ratio of one (1.02), is used as shown in Fig. 4(b), i.e., the blue and red objects initially have similar sizes. After 140 iterations that follow the flow in (20), the size ratio of the two active contours and the distance between mass centers are reconstructed according to the training sample, as shown in Fig. 4(c). Note that the relative orientation of the ellipses is also recovered at steady state, as shown in Fig. 4(d) and Table I.

*4) Coupling Effect in Relative Pose Forces:* Bearing in mind that we have used similar architectures of the gradient flow for coupled shape priors as well as for relative pose priors, in both of these schemes we achieve similar effects of coupling. Following Section II-B, (12) and (20) play similar roles to (8) and (11), respectively, in coupling. In addition, the relative pose variable we estimate here for each structure itself inherently provides a measure of coupling between multiple structures.

### D. Segmentation Algorithm

The overall flow for segmentation involves a weighted sum of flows for the (C&V) data term, the coupled shape prior, and the relative pose prior forces. We represent these forces by modules and illustrate the segmentation algorithm via the diagram in Fig. 5.

In the algorithm, given a test image, initially a set of candidate segmenting contours $\mathbf{C}_{t=0}$ are initialized on it. The initialization method can be either manual or automatic. Then in an iterative process, the curves (surfaces) are deformed by a force which is linear combination of intensity, coupled shape, and relative pose forces that are computed in three different spatial domains, in parallel. As seen in the diagram, we have three curves $\mathbf{C}$, $\tilde{\mathbf{C}}$, and $\bar{\mathbf{C}}$ in different domains. The intensity-based force is computed in the image domain while the prior forces are computed in different domains. The reason is that, we relate candidate segmenting contours to the training set samples of the target objects.

During prior force computations, we relate (align) segmenting contours to the training set samples via $T[\mathbf{p}]$ and $T[p_{glb}]$ operations, where $\tilde{\mathbf{C}} = T[\mathbf{p}]\mathbf{C}$ and $\bar{\mathbf{C}} = T[p_{glb}]\,\mathbf{C}$. The coupled shape pose forces are computed on $\tilde{\mathbf{C}}$ while the relative pose prior forces are computed on $\bar{\mathbf{C}}$. All the computed forces are retranslated into their original image domain for evolution using the transforms $T^{-1}[\mathbf{p}]$ and $T^{-1}[p_{\text{int}}]$ (for details, see Fig. 5). For these alignment (registration) operations, we use the method in [39] described in Appendix D-II in 2-D problems, and a faster method described in Appendix D1 in 3-D problems. Note that the alignment operations take place twice per iteration for each prior computation. In our 3-D experiments, these operations take around 80% of the overall computation time. We provide more details about quantitative analysis of the algorithm when we show experimental results in the following section.

## III. EXPERIMENTAL RESULTS

In this section, we demonstrate the effects of coupled shape and relative pose priors on phantom and real 2-D image slices and real 3-D MR image volumes . We show segmentation results comparing our approach with C&V and the single nonparametric shape prior [41] based methods. We refer to the synergy

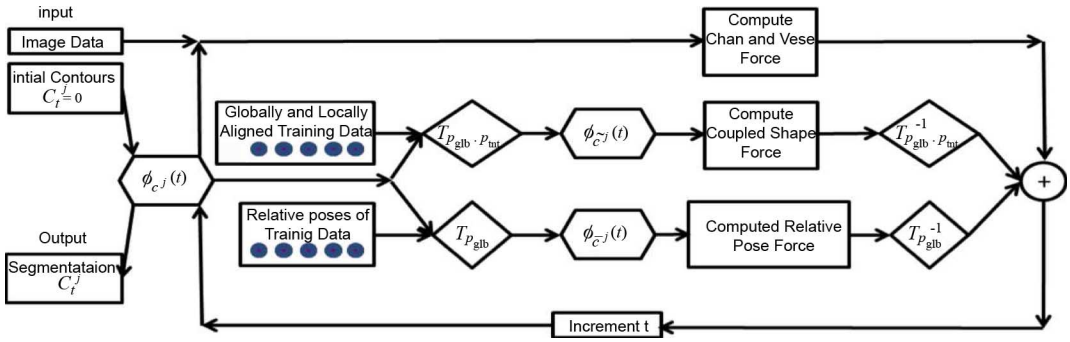


Fig. 5. Segmentation Algorithm—In each step, three forces are evaluated: C&V, coupled shape (see Section II-B), and relative pose (see Section II-C above).

of our coupled shape and relative pose prior based method as one method while it allows for use of the two prior forces separately as well. In addition, we compare our method with state of the art medical image segmentation tools such as FreeSurfer [42], [54] and FSL FIRST [55], [56] used in subcortical segmentation.

We perform a quantitative analysis of the accuracy of the segmentations in terms of false positive rate (FPR) and false negative rate (FNR), (see [65]), Dice error rate $1 - \mathrm{DC}$ (see [66]), and the average surface distance as in [67]. We present 2-D and 3-D experimental results on segmenting the head of Caudate Nucleus, Thalamus, Accumbens Nucleus, Putamen, and Globus Pallidus which are Basal Ganglia structures. For the quantitative analysis and training set building, we use ground truth shapes which are manually segmented by medical experts.[5]

We have utilized various manual and automatic initializations in our experiments. In the 2-D experiments presented here, we have manually initialized the algorithm with a small circle inside each disconnected part of each subcortical structure. In order not to use computational resources for shape and pose prior operations in the initial iterations when the segmenting boundaries is away from the true boundaries, we have run the $C\&V$ flow on these initial boundaries until convergence, and then turned on the forces involved in our technique. In the 3-D case, we have used a number of automatic initialization methods that exploit the training data. In earlier experiments, we have initialized our algorithm with the mean training shape as in [44]. In the 3-D results presented here however, we have used a different approach that picks and uses the boundary of one training sample based on the similarity of the training image to the test image. In particular, we compute the mass centers of the test and the training images, and use the boundaries of the training sample with the closest mass center to the test image as the initializing curves. One could use other simple intensity statistics as a selection criterion as well. Given the fact that our algorithm, just like many active contour-based segmentation algorithms, is based on solving an optimization problem by gradient descent, its final result is expected to have some dependence on the initialization. While detailed experimental analysis of the nature of that dependence is beyond the scope of this paper, our experiments based on the initialization procedures described above have produced reasonable segmentations without significant differences among the results of different initializations and among the computation times. We feel that our coupled priors provide useful constraints on the evolving curves/surfaces to drive them to the true target region faster.

[5]We provide a manual segmentation tool which is freely available at [68]. Basic information about this tool as well as a visual snapshot is provided in Appendix A.

Fig. 6. Ground truth shapes used in creating synthetic images.

Our scheme requires tuning of parameters. In this context, in order to specify the kernel size $\sigma_j$ of the $j\mathrm{th}$ object, we use the maximum likelihood kernel size with leave-one-out method (see [69]). This choice is used for both coupled shape and relative pose priors, which are described in Sections II-B and II-C, respectively.

Theoretically, the running time of the overall algorithm is bounded by $O\left(m^2N\right)$, where m is the number of analyzed structures and $N$ represents the amount of training shapes. The time requirements for the test of segmentation of 2, 3, and 5 structures in 3-D are reported as 15, 30, and 80 s per iteration on a computer with Quad core 2.5 GHz CPU and 4 Gb of RAM, respectively.

### A. Experiments on 2-D Data

*1) Experiments on 2-D Synthetic Data:* In this section, we show 2-D segmentation results on twelve synthetic brain structure images. The synthetic data are created on top of ground truth shapes. The synthetic data consists of ternary images. We use one intensity level for Caudate Nucleus, a second one for Putamen, and the third represents background. The ternary mode allows for simulating variable contrast. We add Gaussian noise on these ternary images. Note that for each brain structure image, we have a ground truth and a noisy ternary image. Ground truths (see Fig. 6) are used for training while noisy ternary data are used for testing.

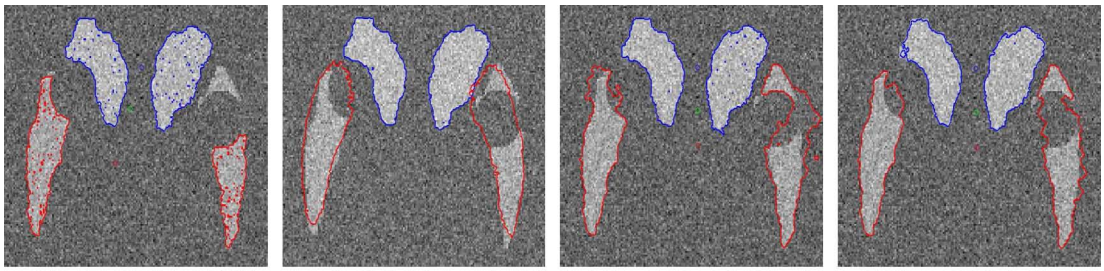

(a) (b) (c) (d)

Fig. 7. Segmentations on synthetic data. (a) C&V method, (b) single shape [41], (c) relative pose (only), (d) proposed coupled shape and relative pose priors.

TABLE II
AVERAGE QUANTITATIVE ACCURACY RESULTS FOR THE EXPERIMENT SHOWN IN FIG. 7

| Prior | Putamen | | |
|---|---|---|---|
| | FPR | FNR | 1-DC |
| Single Shape | 0.0240 | 0.0910 | 0.1770 |
| Coupled Relative Pose | 0.0120 | 0.1830 | 0.1950 |
| Coupled Shape and Relative Pose | 0.0040 | 0.0600 | 0.0700 |

In this context, we have performed a leave one out experiment. In each round, we choose one noisy ternary image for segmentation. The rest of the images, i.e., ground truth shapes, are used in training. We work with high contrasted Caudate Nucleus and low contrasted occluded Putamen, in order to show the effect of using the coupled shape and relative pose priors. The results for one test image are shown in Fig. 7. The C&V method [see Fig. 7(a)] cannot recover the occluded part of Putamen. When using single shape prior of separate objects (see [41]) we obtain a better segmentation result for the occluded part [see Fig. 7(b)]. However, the estimated boundaries for Caudate Nucleus and Putamen overlap. In this experiment, the overlapping is resolved by the relative pose prior scheme [see Fig. 7(c)], although, of course, we do not expect this scheme to recover the shapes very accurately as no priors on shape are used. Nevertheless, this example helps us observe the positive impact of using the relative pose prior. Using coupled shape and relative pose priors together we achieve better segmentation results than all other results, as shown in Fig. 7(d). The coupled shape and relative pose forces expand the contour to cover the bottom parts of the Putamen. These forces also result in better recovery of the occluded regions. In this context, we illustrate the average validation results of Putamen in twelve leave one out experiments (see Table II). All three performance criteria indicate superior accuracy when using coupled shape and relative pose priors together.

*2) Experiments on 2-D Real Data:* In this section, we present segmentation results on real 2-D MR data. In these experiments we use proton density (PD) MR images, although T1 contrast MRI is more commonly used in subcortical structure analysis. The PD modality is interesting to explore because it presents challenging scenarios due to its low contrast. Experiments on T1 contrast images are presented in the next section.

We demonstrate the results of this experiment in Fig. 8. Each method starts with the same initial conditions and we show the results obtained in steady state. We use a training set of twenty binary shapes that comprise the structures of interest, Caudate Nucleus and Putamen. The C&V method results in inevitable leakages (false positives) for both Caudate Nucleus and Putamen [see Fig. 8(a)]. We show the results obtained using single shape priors for separate structures in Fig. 8(b) and (c). For the head of Caudate Nucleus, the single shape prior method presents significant missing (false negatives) and small leakages (false positives) towards the Ventricles. For Putamen, all the segmentation results present lateral leakages. However, the proposed coupled shape prior based approach segments both structures more effectively due to the coupling effect between shapes [see Fig. 8(d)]. We observe that the coupled shape force recovers the missed regions of Caudate Nucleus and provides better accuracy in segmenting the Putamen, as compared to the single shape prior method. The benefit of using a coupled prior is expected to be greater when the boundary of some objects is not well supported by the observed image intensity. This is what we observe through the Putamen results on the given test images. The synergy between the coupled shape and the relative pose forces reduces the overall error further in Caudate Nucleus and Putamen for all images [see Fig. 8(e)]. In these series of experiments, we observe that coupled shape and relative pose priors provide much more structured shape and strong geometry constraints on objects. In particular, the size and the distance constraints between shape pairs, improve the accuracy of the results significantly. We show the achieved average accuracy of the segmentation results from Fig. 8 in Table III.

### B. Experiments on 3-D Real Data

In this section we show results obtained from T1 and T2 contrast 3-D MR images. For the T1 contrast experiments, we use the data set, provided by the IBSR repository[6] [70], in which there are 18 cases, composed of 14 male and 4 female subjects. The range of the age of the group is from 7 to 71 and the slice thickness is 1.5 mm along the coronal section. For the T2 contrast experiments, we used seven cases for which the protocol consisted of spin echo pulse sequence scan in a 3T Philips Achieva machine, with head first-supine (HFS) patient position. The range of the age of the group is from 8 to 55 and the slice thickness is 6 mm along the axial section.

*1) Experiments on 3-D T2-Weighted Real Data:* We used the leave-one out method when preparing the training set for a particular test image. We show the results of the segmentations

[6]"The MR brain data sets and their manual segmentations were provided by the Center for Morphometric Analysis at Massachusetts General Hospital and are available at http://www.cma.mgh.harvard.edu/ibsr/".

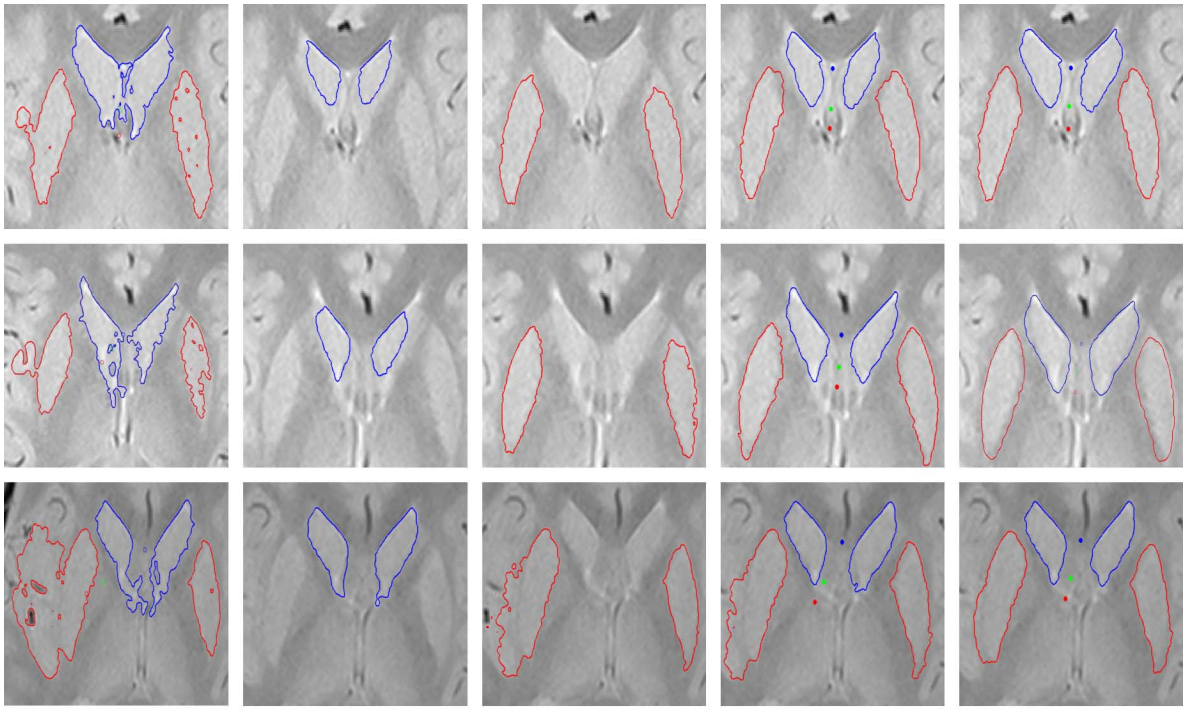


Fig. 8. Segmentation results of the Caudate Nucleus and the Putamen on PD-weighted MR slices. Each row shows segmentation results on a particular test image achieved by different techniques. Each column represents one technique applied on different test images. (a) C&V method. (b) and (c) Single shape prior for separate structures Caudate Nucleus and Putamen. (d) Proposed coupled shape prior (only). (e) Proposed coupled shape and relative pose prior.

TABLE III
AVERAGE QUANTITATIVE ACCURACY RESULTS FOR THE EXPERIMENTS IN FIG. 8

| Prior | Caudate Nucleus 1-DC | Putamen 1-DC |
|---|---|---|
| C&V Force | 0.4200 | 0.3900 |
| Single Shape | 0.1565 | 0.1645 |
| Coupled Shape | 0.1112 | 0.1250 |
| Coupled Shape and Relative Pose | 0.1010 | 0.1220 |

of C&V, the coupled shape prior, and the synergy of coupled shape prior and relative pose prior based methods in Figs. 9–12. We compare the segmentation results of the three methods to ground truths and show superimposed semi-transparent surfaces of segmented structures and ground truths in Fig. 9. We also show all these surfaces separately, in an opaque visualization mode, in Fig. 10. We present the combined result of the multistructure segmentation in Fig. 11. In addition, we show sequences of 2-D slices that intersect the segmentation volumes in Fig. 12. In all the images, we observe that when applying C&V there are serious leakages, for example, in Fig. 11(c) and (d), the left and right Caudate Nucleus overlap. In contrast, when applying coupled shape and relative pose priors, the left and right Caudate Nucleus structures are separate, see, for example, Fig. 11(e)–(h). We present a quantitative evaluation of the accuracies of all methods, in Table IV. Our approach achieves better overall accuracy, i.e., smaller Dice error rates, as compared to existing techniques.

*2) Experiments on 3-D T1-Weighted Real Data:* We have performed experiments on the IBSR data set [70] for joint segmentation of Caudate Nucleus, Putamen, Accumbens Nucleus, Globus Pallidus, and Thalamus. We show one sample result achieved by our approach, together with the ground truth, in Fig. 13. We have tested our algorithm for different number of subcortical structures in the IBSR dataset and analyzed its performance. In particular, we have tested our method on joint segmentation of two structures (Caudate Nucleus and Putamen), three structures (Caudate Nucleus, Putamen, and Thalamus), and all five structures. We have not observed any significant change in the behavior or convergence of our iterative algorithm. We have performed a quantitative comparison of our approach to FreeSurfer and FSL FIRST on the IBSR data set. In Fig. 14, we present the average performance over 10 test cases in terms of the Dice and the average boundary distance measures [67]. Based on these results, FSL FIRST and FreeSurfer perform slightly better than our technique. We should note that both FSL FIRST and FreeSurfer exploit the intensity statistics heavily, whereas our approach uses the simplistic C&V data term, which is not based on learning the intensity statistics from the training data. This is because our objective in this paper has just been to propose and demonstrate a new way of incorporating coupled shape and pose information into the segmentation process. We should also note that the test data used in this experiment was also used in the training of the FSL-FIRST. Despite these facts, our approach achieves comparable performance, which suggests that the benefits provided by our shape and pose priors are significant. We should also note that the versions of FSL FIRST and FreeSurfer we used were tuned to T1 data only, whereas our approach can be applied to any type of data in its current form. One more point is that our approach has a significantly lower computational cost than FreeSurfer (minutes versus hours).

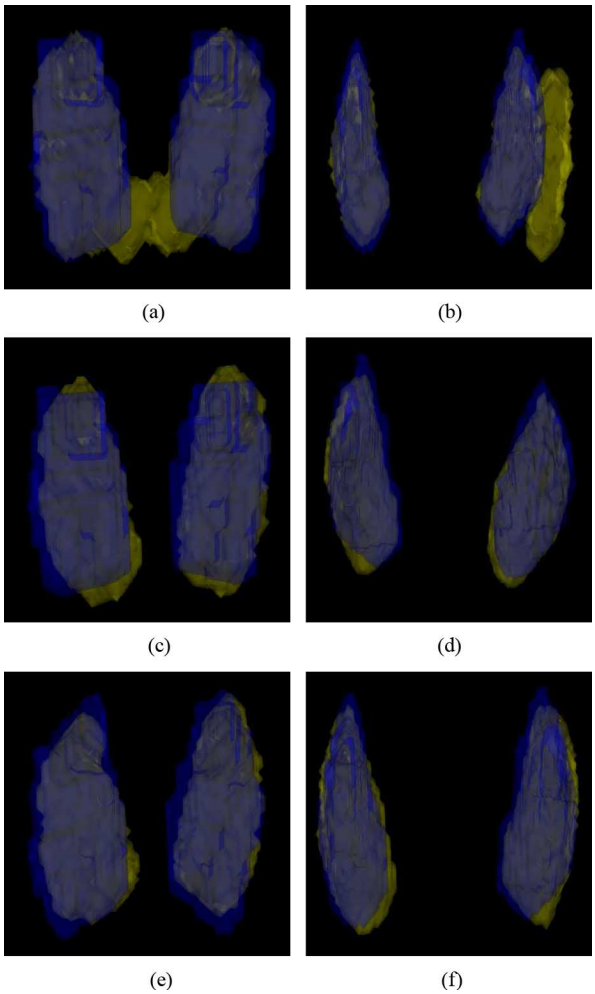


Fig. 9. Comparison of segmentation results to ground truths. The left and right columns represent Caudate Nucleus and Putamen respectively. The segmentation results are shown in yellow and the ground truths are shown in blue. (a) and (b) show the result of C&V. (c) and (d) illustrate the results using the coupled shape prior method. (e) and (f) represent the result employing the shape and relative pose prior scheme.

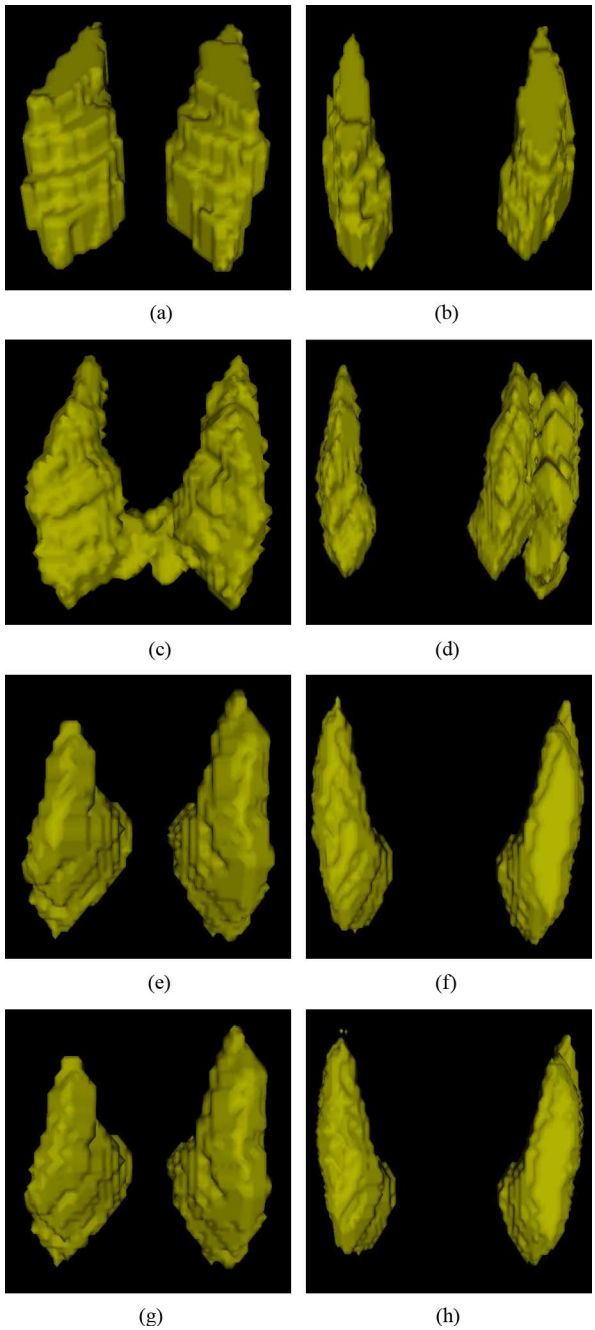


Fig. 10. Comparison of segmentation results to ground truths. The left and right columns represent Caudate Nucleus and Putamen respectively. Figures (a) and (b) show ground truths. Figures (c) and (d) illustrate the segmentation result of C&V. Figures (e) and (f) represent the result achieved using the coupled shape prior method. Figures (g) and (h) show the result obtained employing the shape and relative pose prior scheme.

Our next experiment involves intensity inhomogeneities. In particular, we have tested our technique on perturbed IBSR data with simulated RF overflow artifacts [11]; see Fig. 15 for such sample data. To simulate data with RF overflow artifacts, we consider the coronal plane. For each coronal slice, we multiply the original image with a bias field that is 1 at the center and increases linearly in the horizontal direction. We consider two artifact levels, shown in Fig. 15(b) and (c), where the maximum factor multiplying an intensity is 5 and 10, respectively. In Fig. 16, we show quantitative results based on the Dice score, on data with RF overflow artifacts. In Fig. 16(a), we observe that the proposed method achieves the highest Dice score among the three techniques in the scenario with high RF artifacts. Fig. 16(b) shows how much the three techniques degrade in terms of the Dice score in the presence of RF artifacts. We observe that the proposed technique exhibits robustness to intensity inhomogeneities. This emphasizes the important role played by the coupled shape and relative pose priors in our framework.

In another series of experiments, we have analyzed the sensitivity of the proposed segmentation technique to the number of training shapes. We have considered the problem of segmenting Putamen and Caudate Nucleus in a single test image, and varied the number of training samples from 1 to 17. The results in terms of the Dice coefficient are shown in Fig. 17. We observe a mild trend of increasing accuracy in the results as the number of training shapes are increased.

## IV. Conclusion

We have presented a statistical approach for segmentation of multiple Basal Ganglia structures. We view the segmentation

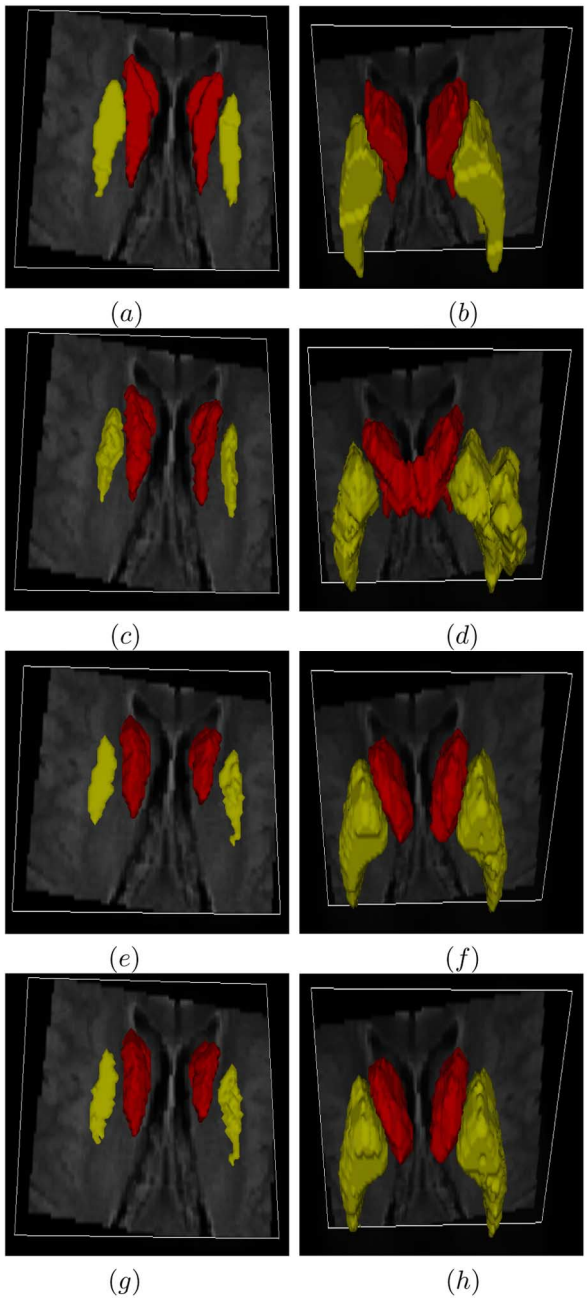


Fig. 11. Comparison of volumetric segmentations from two view-points, downward (left column) and upward (right column). The red and yellow structures represent Caudate Nucleus and Putamen, respectively. Figures (a) and (b) show ground truths. Figures (c) and (d) show the result of C&V. Figures (e) and (f) illustrate the result achieved using the coupled shape prior method. Figures (g) and (h) represent the result achieved using the shape and relative pose prior scheme.

problem in a maximum *a posteriori* (MAP) estimation framework for the unknown boundaries of the anatomical structures. This perspective results in an optimization problem containing multiple terms. We use a standard term for the conditional density of the MR intensity data given the unknown boundaries. Our main contribution however is focused on the prior density terms for the boundaries. Our priors involve joint, coupled densities of multiple structure boundaries. We decompose the boundary information into two parts: shape and pose. We further decompose the pose information into the global pose of the set of structures

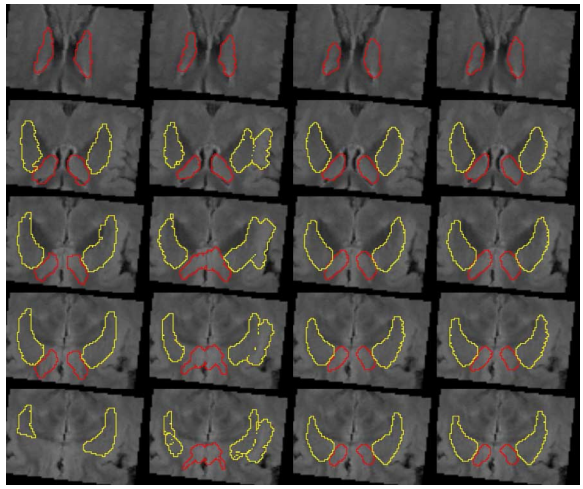

Fig. 12. A comparison of volumetric segmentation results on 2-D axial slides. The red and yellow structures represent Caudate Nucleus and Putamen, respectively. The columns represent ground truths, C&V, coupled shape prior, and coupled shape and pose prior based method segmentation results, from left to right.

TABLE IV
QUANTITATIVE ACCURACY RESULTS FOR THE 3-D EXPERIMENTS IN FIG. 11

| | TPR | FPR | 1 - DC |
|---|---|---|---|
| C&V | 0.7301 | 0.0075 | 0.2680 |
| Coupled Shape | 0.7299 | 0.0050 | 0.2351 |
| Coupled Shape and Relative Pose | 0.7291 | 0.0049 | 0.2335 |

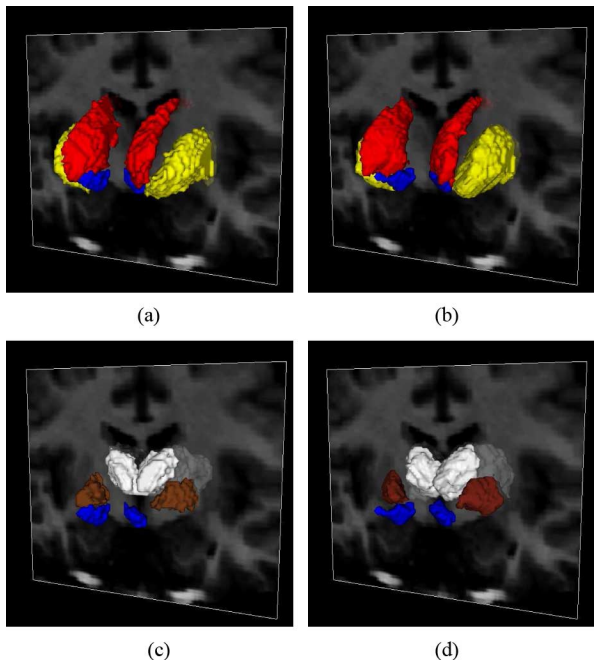


Fig. 13. Five-structure segmentation results on subject IBSR_01 from the IBSR data set. For better visualization the structures are displayed in two groups. Top: Caudate Nucleus (red), Putamen (yellow), Accumbens Nucleus (blue). Bottom: Globus Pallidus (brown), Thalamus (white), Accumbens Nucleus (blue). Left: ground truths. Right: results of proposed approach.

of interest, and the relative (intershape) pose among the structures. We assume we do not have any prior information about the global pose, but rather we exploit the relative pose among the structures. We learn both the joint shapes and the relative poses of the structures from manually-segmented training data

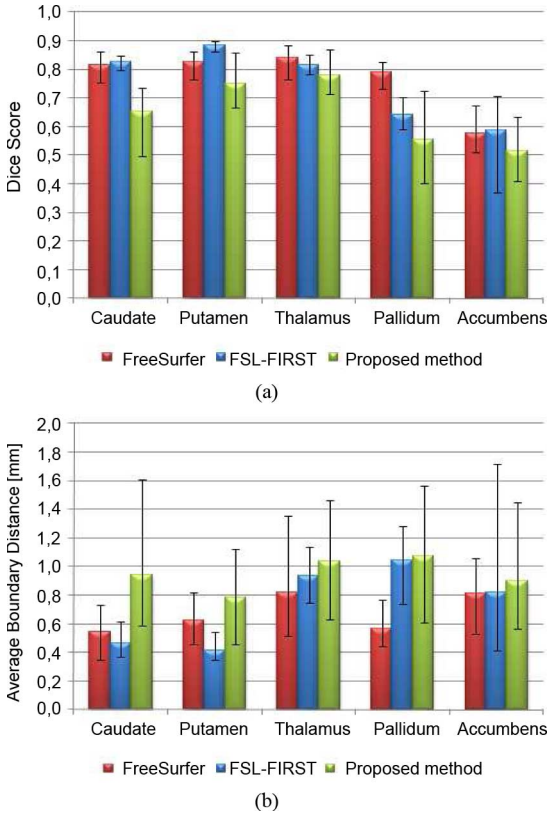


Fig. 14. Quantitative evaluation of the segmentation results on the IBSR data based on (a) the Dice score, and (b) the average surface distance. The colored bars indicate the average score over all test samples while the error bars indicate the maximum and the minimum scores achieved on a test image.

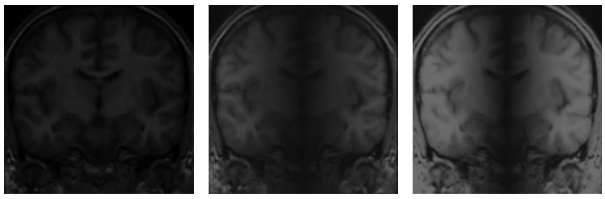


Fig. 15. RF overflow artifacts over the IBSR_01 subject. Original image with no artifacts is shown in (a). Images with RF artifacts where the most distorted pixels are multiplied by factors of 5 and 10 are shown in (b) and (c), respectively.

using nonparametric multivariate kernel density estimation. In this process, we represent boundaries by signed distance functions, and we compute relative poses using moments. We incorporate the learned densities as priors into our MAP estimation framework, and derive the gradient flow expressions for the optimization problem. We implement the gradient flow using an active contour-based iterative algorithm. In the course of this algorithm, we perform appropriate alignment operations between the segmenting curve and the training data. In particular, we perform alignment with respect to global pose, enabling us to evaluate the contribution from the relative pose prior densities; and we also perform alignment with respect to both global and relative pose, enabling us to evaluate the contribution from the joint shape prior densities. This leads to an overall evolution driven by the observed MR data as well as the learned shape and relative pose prior densities. In this way, not only the observed data and the shape prior information about single structures, but also the learned statistical relationships among structures in terms of both shape and pose have an impact on the final segmentation. We present experimental results of segmenting

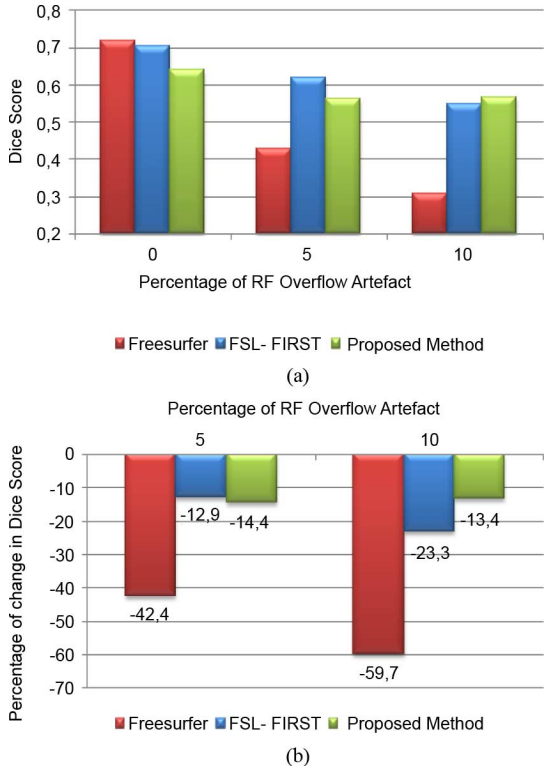


Fig. 16. Performance in the presence of RF overflow artifacts. "0" indicates the case with no artifacts, whereas "5" and "10" correspond to the two levels of RF overflow artifacts described in text. (a) Dice scores. (b) Percentage of change in the Dice scores as compared to the case with no artifacts.

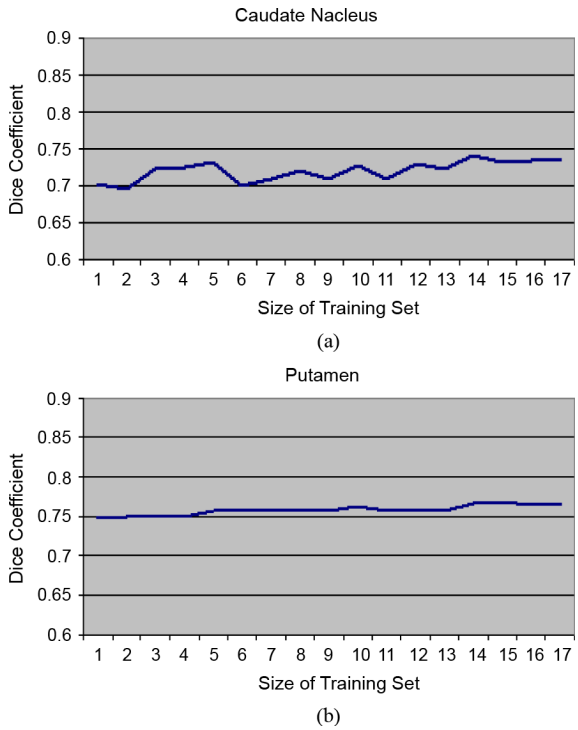


Fig. 17. Sensitivity of the proposed technique to the number of training samples used. Plots show the Dice score achieved on the subject IBSR_01 for (a) Caudate Nucleus and (b) Putamen.

up to five Basal Ganglia structures simultaneously and in a coupled fashion. First we demonstrate the improvement provided by our technique over existing active contour-based methods, especially in challenging scenarios involving data with low contrast, occlusion, or vague structure boundaries. Our quantitative performance analysis supports these observations. Next, we compare our approach to FSL FIRST and FreeSurfer. Although our approach does not exploit the intensity statistics of the data, it achieves comparable performance. Furthermore, on data corrupted by intensity inhomogeneities, our technique appears to be more robust. The proposed approach could also be applied to segmenting other basal ganglia structures, or in fact to any other segmentation problem involving any number of multiple, coupled objects. One could improve upon our experimental results by using a learning-based data term in our framework, that could potentially model the intensity characteristics more accurately.

Further experimental analysis of our approach could involve data of normal and diseased subjects. When such data are included in the training set, our approach will be able to exploit that. Furthermore we should note that the nonparametric density estimation structure allows our approach to learn multimodal densities. Hence, in the process of segmenting a test image given a training population involving multiple "subclasses" of data (e.g., normal and diseased), our approach should automatically guide the segmentation towards one of the "subclasses" in the prior. Even further analysis could involve testing the behavior of the algorithm when the test subject belongs to a "subclass" not included in the training set.

## APPENDIX

*A) Implementation Details and 3-D Ground Truth Labeling:* We provide a 3-D image editor for creating and visualizing ground truths of anatomical structures in medical images. A snapshot of the application program is shown in Fig. 18. This editor is able to read data in DICOM (see [71]) and Analyze (see [72]) formats. The manual labeling of the structures is performed by using spline contours which are drawn along the boundary of the target objects. The user goes through the slices of the volume, and at each level depicts the splines. Once all the slices are finished, inside of the contours are filled and the slices are merged to result in a labeled volume. Splines are implemented using vtkSplineWidget class (see [73]) and visualization methods are implemented using VTK library [74]. The open-source code and more details are freely available at [68].

The level set based segmentation framework has been implemented using ITK [75], which is a publicly available tool that provides C++ libraries in an object oriented framework. We have built our segmentation modules as inherited from ITK level set framework which provides an optimized (fast) curve evolution algorithm in 3-D.

*B) Computation of the Coupled Shape Prior Flow:* In this section, we describe the computation of the gradient flow of $\log P\left(\tilde{\mathbf{C}}\right)$. From (8), we have

$$\log P\left(\tilde{\mathbf{C}}\right) = \log \frac{1}{N}\sum_{i=1}^{N}\prod_{j=1}^{m} k\left(d_{L_2}(\phi_{\tilde{C}^j}, \phi_{\tilde{C}_i^j}), \sigma_j\right) = \log \frac{1}{N}\sum_{i=1}^{N}\prod_{j=1}^{m} k_i^j \tag{22}$$

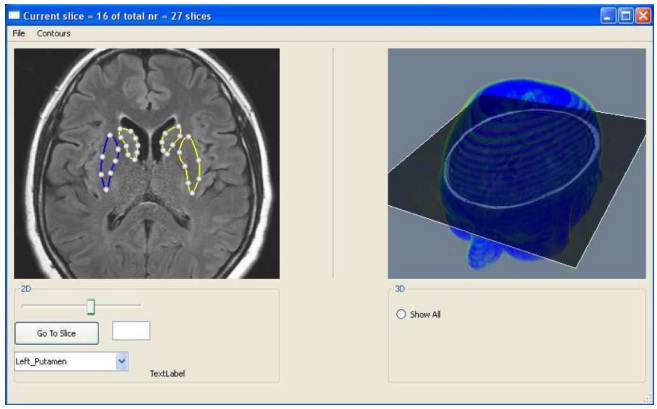


Fig. 18. 3-D ground truth editor. The left window is a 2-D sectioning plane where the user can use drawing tools. On the right window, the current plane on the left is superimposed to the volumetric data, in order to provide 3-D positioning information.

where $\phi_{\tilde{C}_i^j}$ is the signed distance function for the $i$th training shape and the $j$th object. Note that $\phi_{\tilde{C}^j}$ is a function of time $t$.

*1) Derivation of the Coupled Shape Prior Evolution Formula:* Consider the derivative of the product of kernels

$$\frac{\partial}{\partial t}\prod_{j=1}^{m} k_i^j = \sum_{j=1}^{m} k_i^{j'} \prod_{l=1, l\neq j}^{m} k_i^l.$$

Then

$$\frac{\partial}{\partial t}\log P\left(\tilde{\mathbf{C}}\right) = \frac{1}{P\left(\tilde{\mathbf{C}}\right)}\frac{1}{N}\sum_{i=1}^{N}\sum_{j=1}^{m} k_i^{j'} \prod_{l=1, l\neq j}^{m} k_i^l. \tag{23}$$

Next, consider the derivatives of the kernels

$$k_i^{j'} = k_i^j\left\{-\frac{1}{2{\sigma_j}^2}\int_{\Omega} 2\left(\phi_{\tilde{C}^j}(\mathrm{x}) - \phi_{\tilde{C}_i^j}(\mathrm{x})\right)\frac{\partial \phi_{\tilde{C}^j}}{\partial t}(\mathrm{x})\, d\mathrm{x}\right\} \tag{24}$$

where x denotes the position vector. Substituting (24) into (23), we obtain

$$\frac{\partial}{\partial t}\log P\left(\tilde{\mathbf{C}}\right) = -\frac{1}{P\left(\tilde{\mathbf{C}}\right)}\frac{1}{N}\sum_{i=1}^{N} \left\{\left(\prod_{l=1}^{m} k_i^l\right)\sum_{j=1}^{m}\left[\frac{1}{2{\sigma_j}^2}\cdot\int_{\Omega} 2\left(\phi_{\tilde{C}^j}(\mathrm{x}) - \phi_{\tilde{C}_i^j}(\mathrm{x})\right)\frac{\partial \phi_{\tilde{C}^j}}{\partial t}(\mathrm{x})\, d\mathrm{x}\right]\right\}.$$

Since $k_i^j$ are common multipliers

$$\frac{\partial}{\partial t}\log P\left(\tilde{\mathbf{C}}\right) = -\frac{1}{P\left(\tilde{\mathbf{C}}\right)}\frac{1}{N}\sum_{i=1}^{N}\left(\prod_{l=1}^{m} k_i^l\right) \times\left[\sum_{j=1}^{m}\frac{1}{2{\sigma_j}^2}\cdot\int_{\Omega} 2\left(\phi_{\tilde{C}^j}(\mathrm{x}) - \phi_{\tilde{C}_i^j}(\mathrm{x})\right)\frac{\partial \phi_{\tilde{C}^j}}{\partial t}(\mathrm{x})\, d\mathrm{x}\right]. \tag{25}$$

Employing the inner product

$$\langle \phi_1, \phi_2\rangle = \int_{\Omega} \phi_1(\mathrm{x})\,\phi_2(\mathrm{x})\, d\mathrm{x}$$

and (25) we have

$$\frac{\partial}{\partial t}\log\left(P\left(\tilde{\mathbf{C}}\right)\right) = \frac{1}{P\left(\tilde{\mathbf{C}}\right)}\frac{1}{N}\sum_{i=1}^{N}\left(\prod_{l=1}^{m}k_i^l\right) \sum_{j=1}^{m}\left\{\frac{1}{{\sigma_l}^2}\left\langle\left(\phi_{\tilde{C_i^j}}(\mathrm{x})-\phi_{\tilde{C}^j}(\mathrm{x})\right),\frac{\partial\phi_{\tilde{C}^j}}{\partial t}(\mathrm{x})\right\rangle\right\} = \sum_{j=1}^{m}\left\langle\frac{1}{P\left(\tilde{\mathbf{C}}\right)}\frac{1}{N}\sum_{i=1}^{N}\left(\prod_{l=1}^{m}k_i^l\right)\left\{\frac{1}{{\sigma_j}^2}\left(\phi_{\tilde{C_i^j}}(\mathrm{x})-\phi_{\tilde{C}^j}(\mathrm{x})\right)\right\},\frac{\partial\phi_{\tilde{C}^j}}{\partial t}(\mathrm{x})\right\rangle.$$

In order to maximize (22), we evaluate gradient directions, which assure the fastest increase of the functional $\log P\left(\tilde{\mathbf{C}}\right)$ for each object contour. The gradient directions for the contours $\tilde{C}^j$ are

$$\frac{\partial\phi_{\tilde{C}^j}}{\partial t} = \frac{1}{P\left(\tilde{\mathbf{C}}\right)}\frac{1}{N}\sum_{i=1}^{N}\left(\prod_{l=1}^{m}k_i^l\right)\cdot\frac{1}{{\sigma_j}^2}\left(\phi_{\tilde{C_i^j}}(\mathrm{x})-\phi_{\tilde{C}^j}(\mathrm{x})\right). \quad (26)$$

*2) Coupling Effect of Multiple Shapes:* The set of (26) impose that the active contours evolve toward shapes that manifest local maximum of objects' joint shape prior. At the local maximum of the joint shape prior $P\left(\tilde{\mathbf{C}}\right)$, the gradient flow is zero, i.e., at the steady state, when the joint shape prior is maximum, there is no flow (for any of the $m$ contours). At steady state, we have

$$\frac{\partial\phi_{\tilde{C}^j}}{\partial t} = \frac{1}{P\left(\tilde{\mathbf{C}}\right)N}\sum_{i=1}^{N}\prod_{l=1}^{m}k_i^l\frac{1}{{\sigma_j}^2}\times\left(\phi_{\tilde{C_i^j}}(\mathrm{x})-\phi_{\tilde{C}^j}(\mathrm{x})\right)=0$$

where x denotes the position vector. Therefore, we impose the following constraints:

$$\frac{\partial\phi_{\tilde{C}^j}}{\partial t} = \frac{1}{{\sigma_j}^2}\sum_{i=1}^{N}\lambda_i\left(\tilde{\mathbf{C}}\right)\left(\phi_{\tilde{C_i^j}}(\mathrm{x})-\phi_{\tilde{C}^j}(\mathrm{x})\right)=0, \quad (27)$$

where $\lambda_i\left(\tilde{\mathbf{C}}\right) = \prod_{j=1}^{m}k_i^j/NP\left(\tilde{\mathbf{C}}\right)$ Note that, $P\left(\tilde{\mathbf{C}}\right) = 1/N\sum_{i=1}^{N}\prod_{j=1}^{m}k_i^j$ and thus $\sum_{i=1}^{N}\lambda_i\left(\tilde{\mathbf{C}}\right)=1$.

The set of (27) are equivalent with (11). Then, the coupled shapes at the local maximum satisfy

$$\phi_{\tilde{C}^j}(\mathrm{x}) = \frac{1}{N}\sum_{i=1}^{N}\lambda_i\left(\tilde{\mathbf{C}}\right)\phi_{\tilde{C_i^j}}(\mathrm{x}).$$

*C) Analytical Computation of Relative Pose Prior Flow:* Without loss of generality, in this Appendix, we present formulae for $\theta_z$ processing. The cases $\theta_x$ and $\theta_y$ are similar. During the evolution of active contours, the relative pose parameters depend on time. Therefore, from (18), we have

$$\theta_z(C) = \frac{1}{2}\arctan\left(\frac{2\left(m_{1,0,0}(t)\,m_{0,1,0}(t)-m_{1,1,0}(t)\,m_{0,0,0}(t)\right)}{\left(m_{0,2,0}(t)-m_{2,0,0}(t)\right)m_{0,0,0}(t)+m_{1,0,0}^2(t)-m_{0,1,0}^2(t)}\right). \quad (28)$$

Define

$$un\_\sin(2\theta_z) = 2\left(m_{1,0,0}(t)\,m_{0,1,0}(t)-m_{1,1,0}(t)\,m_{0,0,0}(t)\right)$$

and

$$un\_\cos(2\theta_z) = \left(m_{0,2,0}(t)-m_{2,0,0}(t)\right)m_{0,0,0}(t) + m_{1,0,0}^2(t)-m_{0,1,0}^2(t). \quad (29)$$

In addition, let $S>0$ and $un\_\sin^2(2\theta_z)+un\_\cos^2(2\theta_z)=S^2$. With these notations, we have the following interpretations: $un\_\sin(2\theta_z)=S\sin(2\theta_z)$ and $un\_\cos(2\theta_z)=S\cos(2\theta_z)$.

In the following, we develop the derivative of the orientation angle with respect to time. We use trigonometric relationships to model the moment based expressions, while keeping in mind their dependence on time. Therefore, we have

$$\begin{aligned}
&\theta_z(C)' \\
=&\frac{1}{2}\frac{\tan'(2\theta_z)}{1+\tan^2(2\theta_z)} \\
=&\frac{1}{2}\frac{un_\sin'(2\theta_z)\,un_\cos(2\theta_z)-un_\sin(2\theta_z)\,un_\cos'(2\theta_z)}{un_\cos^2(2\theta_z)\left(1+\tan^2(2\theta_z)\right)} \\
=&\frac{1}{2}\frac{\left(un_\sin'(2\theta_z)\,un_\cos(2\theta_z)-un_\sin(2\theta_z)\,un_\cos'(2\theta_z)\right)}{S^2}\cdot \\
=&\left[\left(m'_{1,0,0}(t)\,m_{0,1,0}(t)+m'_{0,1,0}(t)\,m_{1,0,0}(t)\right.\right. \\
&\quad -m'_{1,1,0}(t)\,m_{0,0,0}(t) \\
&\left.-m'_{0,0,0}(t)\,m_{1,1,0}(t)\right)\frac{\cos(2\theta_z)}{S} \\
&-\left(\left(m'_{0,2,0}(t)-m'_{2,0,0}(t)\right)m_{0,0,0}(t)+\right. \\
&\quad \left(m_{0,2,0}(t)-m_{2,0,0}(t)\right)m'_{0,0,0}(t)+2m'_{1,0,0}(t) \\
&\left.\left.m_{1,0,0}(t)-2m'_{0,1,0}(t)\,m_{0,1,0}(t)\right)\frac{\sin(2\theta_z)}{2S}\right] \\
=&\left[\left(m'_{1,0,0}m_{0,1,0}+m'_{0,1,0}m_{1,0,0}-m'_{1,1,0}m_{0,0,0}-m'_{0,0,0}m_{1,1,0}\right)\right. \\
&\frac{\cos(2\theta_z)}{S}-\left(\left(m'_{0,2,0}-m'_{2,0,0}\right)m_{0,0,0}+\left(m_{0,2,0}-m_{2,0,0}\right)\right. \\
&\left.\left.m'_{0,0,0}+2m'_{1,0,0}m_{1,0,0}-2m'_{0,1,0}m_{0,1,0}\right)\frac{\sin(2\theta_z)}{2S}\right] \\
=&\left\{m'_{0,0,0}\left[\left(m_{2,0,0}-m_{0,2,0}\right)\frac{\sin(2\theta_z)}{2S}-m_{1,1,0}\frac{\cos(2\theta_z)}{S}\right]\right.
\end{aligned}$$

$$+m'_{1,0,0}\left[m_{0,1,0}\frac{\cos(2\theta_z)}{S}-m_{1,0,0}\frac{\sin(2\theta_z)}{S}\right]$$
$$+m'_{0,1,0}\left[m_{1,0,0}\frac{\cos(2\theta_z)}{S}+m_{0,1,0}\frac{\sin(2\theta_z)}{S}\right]$$
$$-m'_{0,2,0}m_{0,0,0}\frac{\sin(2\theta_z)}{2S}+m'_{2,0,0}m_{0,0,0}\frac{\sin(2\theta_z)}{2S}$$
$$-m'_{1,1,0}m_{0,0,0}\frac{\cos(2\theta_z)}{S}\Bigg\}. \quad (30)$$

Define the following coefficients:

$$\begin{aligned}
M^{\theta_z}_{0,0}&=(m_{2,0,0}-m_{0,2,0})\frac{\sin(2\theta_z)}{2S}-m_{1,1,0}\frac{\cos(2\theta_z)}{S}\\
M^{\theta_z}_{1,0}&=m_{0,1,0}\frac{\cos(2\theta_z)}{S}-m_{1,0,0}\frac{\sin(2\theta_z)}{S}\\
M^{\theta_z}_{0,1}&=m_{1,0,0}\frac{\cos(2\theta_z)}{S}+m_{0,1,0}\frac{\sin(2\theta_z)}{S}\\
M^{\theta_z}_{2,0}&=m_{0,0,0}\frac{\sin(2\theta_z)}{2S}\\
M^{z\theta_z}_{0,2}&=-m_{0,0,0}\frac{\sin(2\theta_z)}{2S}\\
M^{\theta_z}_{1,1}&=-m_{0,0,0}\frac{\cos(2\theta_z)}{S}. \quad (31)
\end{aligned}$$

Then, by substituting (31) into (30), we have

$$\theta_z(C)'=\sum_{r=0}^{2}\sum_{s=0}^{2-r}m'_{r,s,0}M^{\theta_z}_{rs}. \quad (32)$$

Further, substituting (32) in (19), we have

$$\begin{aligned}
k_i^{j\prime}=&\\
&k_i^j\Bigg\{-\frac{1}{{\sigma_j}^2}\Bigg[\left(m_{0,0,0}(\bar{C}^j)-m_{0,0,0}\left(\bar{C}_i^j\right)\right)\frac{\partial m_{0,0,0}(\bar{C}^j)}{\partial t}\\
&\quad+\sum_{m^j_{r,s,t}\in\mathcal{M}_2,r+s+t=1}\left(\frac{m_{r,s,t}(\bar{C}^j)}{m_{0,0,0}(\bar{C}^j)}-\frac{m_{r,s,t}\left(\bar{C}_i^j\right)}{m_{0,0,0}\left(\bar{C}_i^j\right)}\right)\\
&\quad\cdot\frac{\partial}{\partial t}\left(\frac{m_{r,s,t}(\bar{C}^j)}{m_{0,0,0}(\bar{C}^j)}\right)+\left(\theta_x(\bar{C}^j)-\theta_x\left(\bar{C}_i^j\right)\right)\frac{\partial}{\partial t}\theta_x(\bar{C}^j)\\
&\quad+\left(\theta_y(\bar{C}^j)-\theta_y\left(\bar{C}_i^j\right)\right)\frac{\partial}{\partial t}\theta_y(\bar{C}^j)\\
&\quad+\left(\theta_z(\bar{C}^j)-\theta_z\left(\bar{C}_i^j\right)\right)\frac{\partial}{\partial t}\theta_z(\bar{C}^j)\Bigg]\Bigg\}\\
=&k_i^j\Bigg\{-\frac{1}{{\sigma_j}^2}\Bigg[\left(m^j_{0,0,0}-m^{ji}_{0,0,0}\right)\frac{\partial m^j_{0,0,0}}{\partial t}\\
&\quad\cdot+\sum_{m^j_{r,s,t}\in\mathcal{M}_2,r+s+t=1}\left(\frac{m_{r,s,t}{}^j}{m_{0,0,0}}-\frac{m^{ji}_{r,s,t}}{m^{i}_{0,0,0}}\right)\frac{\partial}{\partial t}\left(\frac{m^j_{r,s,t}}{m_{0,0,0}}\right)\\
&\quad+\left(\bar{\theta}^j_x-\bar{\theta}^{ji}_x\right)\frac{\partial\bar{\theta}^j_x}{\partial t}+\left(\bar{\theta}^j_y-\bar{\theta}^{ji}_y\right)\frac{\partial\bar{\theta}^j_y}{\partial t}+\left(\bar{\theta}^j_z-\bar{\theta}^{ji}_z\right)\frac{\partial\bar{\theta}^j_z}{\partial t}\Bigg]\Bigg\}\\
=&k_i^j\Bigg\{-\frac{1}{{\sigma_j}^2}\Bigg[\left(m^j_{0,0,0}-m^{ji}_{0,0,0}\right)m_{0,0,0}{}^{j'}\\
&\quad\cdot+\sum_{m^j_{r,s,t}\in\mathcal{M}_2,r+s+t=1}\left(\frac{m^j_{r,s,t}}{m^j_{0,0,0}}-\frac{m^{ji}_{r,s,t}}{m^{ji}_{0,0,0}}\right)\\
&\quad\cdot\left(\frac{m^j_{r,s,t}{}'m^j_{0,0,0}-m^j_{r,s,t}m^j_{0,0,0}{}'}{\left(m^j_{0,0,0}\right)^2}\right)\\
&\quad\cdot+\left(\bar{\theta}^j_x-\bar{\theta}^{ji}_x\right)\sum_{s=0}^{2}\sum_{t=0}^{2-s}m^{j'}_{0,s,t}M^{\theta_x j}_{st}\\
&\quad+\left(\bar{\theta}^j_y-\bar{\theta}^{ji}_y\right)\sum_{r=0}^{2}\sum_{t=0}^{2-r}m^{j'}_{r,0,t}M^{\theta_y j}_{rt}+\\
&\quad\cdot\left(\bar{\theta}^j_z-\bar{\theta}^{ji}_z\right)\sum_{r=0}^{2}\sum_{s=0}^{2-r}m^{j'}_{r,s,0}M^{\theta_z j}_{rs}\Bigg]\Bigg\}.
\end{aligned}$$

Therefore, we have

$$\begin{aligned}
&k_i^{j\prime}\\
&k_i^j\Bigg\{\frac{1}{{\sigma_j}^2}\Bigg[\left(m^j_{0,0,0}-m^{ji}_{0,0,0}\right)\int_{R^3}\phi'_{\bar{C}^j}\phi'_{\bar{C}^j}\delta_\epsilon(\phi_{\bar{C}^j})\,dxdydz\\
&\quad+\sum_{m^j_{r,s,t}\in\mathcal{M}_2,r+s+t=1}\left(\frac{m^j_{r,s,0}}{m^j_{0,0,0}}-\frac{m^{ji}_{r,s,0}}{m^{ji}_{0,0,0}}\right)\\
&\quad\cdot\left(\frac{\int_{R^3}\left(x^ry^sz^tm^j_{0,0,0}-m^j_{r,s,t}\right)\phi'_{\bar{C}^j}\delta_\epsilon(\phi_{\bar{C}^j})\,dxdydz}{\left(m^j_{0,0,0}\right)^2}\right)\\
&\quad+\left(\bar{\theta}^j_x-\bar{\theta}^{ji}_x\right)\sum_{s=0}^{2}\sum_{t=0}^{2-s}\int_{R^3}y^sz^t\phi'_{\bar{C}^j}M^{\theta_x j}_{st}\delta_\epsilon(\phi_{\bar{C}^j})dxdydz\\
&\quad+\left(\bar{\theta}^j_y-\bar{\theta}^{ji}_y\right)\sum_{r=0}^{2}\sum_{t=0}^{2-r}\int_{R^3}x^rz^t\phi'_{\bar{C}^j}M^{\theta_y j}_{rt}\delta_\epsilon(\phi_{\bar{C}^j})dxdydz\\
&\quad+\left(\bar{\theta}^j_z-\bar{\theta}^{ji}_z\right)\sum_{r=0}^{2}\sum_{s=0}^{2-r}\int_{R^3}x^ry^s\phi'_{\bar{C}^j}M^{\theta_z j}_{rs}\delta_\epsilon(\phi_{\bar{C}^j})dxdydz\Bigg]\Bigg\}\\
&=k_i^j\Bigg\{\frac{1}{{\sigma_j}^2}\Bigg[\left(m^j_{0,0,0}-m_{0,0,0}{}^{ji}\right)\left\langle\delta_\epsilon(\phi_{\bar{C}^j}),\phi'_{\bar{C}^j}\right\rangle\\
&\quad+\sum_{m^j_{r,s,t}\in\mathcal{M}_2,r+s+t=1}\left(\frac{m^j_{r,s,t}}{m^j_{0,0,0}}-\frac{m_{r,s,t}{}^{ji}}{m_{0,0,0}{}^{ji}}\right)\\
&\quad\cdot\left\langle\frac{\left(x^ry^sz^tm^j_{0,0,0}-m^j_{r,s,t}\right)}{\left(m^j_{0,0,0}\right)^2}\delta_\epsilon(\phi_{\bar{C}^j}),\phi'_{\bar{C}^j}\right\rangle\\
&\quad+\left(\bar{\theta}^j_x-\bar{\theta}^{ji}_x\right)\sum_{s=0}^{2}\sum_{t=0}^{2-s}\left\langle y^sz^tM^{\theta_x}_{st}\delta_\epsilon(\phi_{\bar{C}^j}),\phi'_{\bar{C}^j}\right\rangle\\
&\quad+\left(\bar{\theta}^j_y-\bar{\theta}^{ji}_y\right)\sum_{r=0}^{2}\sum_{t=0}^{2-r}\left\langle x^rz^tM^{\theta_y}_{rt}\delta_\epsilon(\phi_{\bar{C}^j}),\phi'_{\bar{C}^j}\right\rangle\\
&\quad+\left(\bar{\theta}^j_z-\bar{\theta}^{ji}_z\right)\sum_{r=0}^{2}\sum_{s=0}^{2-r}\left\langle x^ry^sM^{\theta_z}_{rs}\delta_\epsilon(\phi_{\bar{C}^j}),\phi'_{\bar{C}^j}\right\rangle\Bigg]\Bigg\}
\end{aligned}$$

$$
\begin{aligned}
&= k_i^j \left\{ \left\langle \frac{1}{{\sigma_j}^2} \left[ \left( m_{0,0,0}^j - m_{0,0,0}^{ji} \right) + \right. \right. \right. \\
&\quad \cdot \sum_{m_{r,s,t}^j \in \mathcal{M}_2, r+s+t=1} \left( \frac{m_{r,s,t}^j}{m_{0,0,0}^j} - \frac{m_{r,s,t}{}^{ji}}{m_{0,0,0}{}^{ji}} \right) \\
&\quad \cdot \frac{\left( x^r y^s m_{0,0,0}^j - m_{r,s,t}^j \right)}{\left( m_{0,0,0}^j \right)^2} \\
&\quad + \left( \bar{\theta}_x^j - \bar{\theta}_x^{ji} \right) \sum_{s=0}^{2} \sum_{t=0}^{2-s} y^s z^t M_{st}^{\theta_x j} \delta_\epsilon \left( \phi_{\bar{C}^j} \right), \phi'_{\bar{C}^j} + \\
&\left( \bar{\theta}_y^j - \bar{\theta}_y^{ji} \right) \sum_{r=0}^{2} \sum_{t=0}^{2-r} x^r z^t M_{rt}^{\theta_y j} \delta_\epsilon \left( \phi_{\bar{C}^j} \right), \phi'_{\bar{C}^j} \\
&\quad \left. \left. + \left( \bar{\theta}_z^j - \bar{\theta}_z^{ji} \right) \sum_{s=0}^{2} \sum_{s=0}^{2-s} x^r y^s M_{rs}^{\theta_z j} \right] \delta_\epsilon \left( \phi_{\bar{C}^j} \right), \phi'_{\bar{C}^j} \right\rangle \right\}.
\end{aligned}
$$

Note that we use index $j$ to represent the anatomical structures of interest and use index $i$ to iterate over the training set. For example, if the multistructure ensemble consists of Caudate Nucleus and Putamen, then $m = 2$, and $j \in \{1, 2\}$. Although $i$ and $j$ appear as upper script indices, they are not powers. Note also that in these derivations, we have neglected the weights involved in the distance computation for notational simplicity.

Define the moments pose force (MPF) of the $j$th object as

$$
\begin{aligned}
&\mathrm{MPF}\,(j,i) \\
&\quad = \left( m_{0,0,0}^j - m_{0,0,0}{}^{ji} \right) \\
&\qquad + \sum_{m_{r,s,t}^j \in \mathcal{M}_2, r+s+t=1} \left( \frac{m_{r,s,t}^j}{m_{0,0,0}^j} - \frac{m_{r,s,t}{}^{ji}}{m_{0,0,0}{}^{ji}} \right) \\
&\qquad \cdot \frac{\left( x^r y^s z^t m_{0,0,0}^j - m_{r,s,t}^j \right)}{\left( m_{0,0,0}^j \right)^2} \\
&\qquad + \left( \bar{\theta}_x^j - \bar{\theta}_x^{ji} \right) \sum_{s=0}^{2} \sum_{t=0}^{2-s} y^s z^t M_{st}^{\theta_x j} \\
&\qquad + \left( \bar{\theta}_y^j - \bar{\theta}_y^{ji} \right) \sum_{r=0}^{2} \sum_{t=0}^{2-r} x^r z^t M_{rt}^{\theta_y j} \\
&\qquad + \left( \bar{\theta}_z^j - \bar{\theta}_z^{ji} \right) \sum_{r=0}^{2} \sum_{s=0}^{2-r} x^r y^s M_{rs}^{\theta_z j}. \qquad (33)
\end{aligned}
$$

Equation (33) is identical to (21) when we add in the neglected weights. With this notation, we have

$$
\begin{aligned}
&\frac{\partial}{\partial t} \log P \left( \bar{\mathbf{C}} | \tilde{\mathbf{C}} \right) \\
&\qquad = \sum_{j=1}^{m} \left\langle \frac{\sum_{i=1}^{N} \frac{\prod_{l=1}^{m} k_i^l}{{\sigma_j}^2} \mathrm{MPF}\,(j,i)\, \delta_\epsilon \left( \phi_{\bar{C}^j} \right)}{P \left( \bar{\mathbf{C}} | \tilde{\mathbf{C}} \right) \cdot N}, \frac{\partial \phi_{\bar{C}^j}}{\partial t} \right\rangle.
\end{aligned}
$$

We define the $m$-uples

$$
\begin{aligned}
&\left( \frac{\sum_{i=1}^{N} \frac{\prod_{l=1}^{m} k_i^l}{{\sigma_1}^2} MPF\,(1,i)\, \delta_\epsilon \left( \phi_{\bar{C}^1} \right)}{P \left( \bar{\mathbf{C}} | \tilde{\mathbf{C}} \right) \cdot N}, \right. \\
&\frac{\sum_{i=1}^{N} \frac{\prod_{l=1}^{m} k_i^l}{{\sigma_2}^2} \mathrm{MPF}\,(2,i)\, \delta_\epsilon \left( \phi_{\bar{C}^2} \right)}{P \left( \bar{\mathbf{C}} | \tilde{\mathbf{C}} \right) \cdot N}, \ldots \\
&\left. \frac{\sum_{i=1}^{N} \frac{\prod_{l=1}^{m} k_i^l}{{\sigma_m}^2} MPF\,(m,i)\, \delta_\epsilon \left( \phi_{\bar{C}^m} \right)}{P \left( \bar{\mathbf{C}} | \tilde{\mathbf{C}} \right) \cdot N} \right)
\end{aligned}
$$

and $(\partial \phi_{\bar{C}^1}/\partial t, \partial \phi_{\bar{C}^2}/\partial t, \ldots, \partial \phi_{\bar{C}^m}/\partial t)$ as vector valued update per each pixel. Therefore,

$$
\frac{\partial \phi_{\bar{C}^j}}{\partial t}(x,y) = \frac{\sum_{i=1}^{N} \frac{\prod_{l=1}^{m} k_i^l}{{\sigma_j}^2} \mathrm{MPF}\,(j,i)\, \delta_\epsilon \left( \phi_{\bar{C}^j} \right)}{P \left( \bar{\mathbf{C}} | \tilde{\mathbf{C}} \right) \cdot N} \qquad (34)
$$

defines the fastest evolution. The set of (34) are identical to (20).

*D) Registration Details:* In this Appendix, we provide the details of the registration methods we have used. Let $I$ be an image that is to be registered, or source image. Let this image be embedded in the continuous domain $\Omega$, i.e., for any $x \in \Omega$, $I(x)$ represents a pixel $\left(\Omega \subseteq R^2\right)$ or a voxel $\left(\Omega \subseteq R^3\right)$ value. Let $\tilde{I}$ be the registration result, or a target image. We model registration by a similarity transformation $T[\mathbf{p}]$ with the pose parameter $\mathbf{p}$ consisting of translation, rotation, and scaling.

The transformation of $I(x)$ is defined to be the new image obtained by moving every pixel/voxel $(x)$ of the image $I$ to a new position $T[\mathbf{p}](x)$ making the intensity of $\tilde{I}$ at pixel/voxel $T[\mathbf{p}](x)$ the same as the intensity of $I$ at location $x$. Thus the two images $I$ and $\tilde{I} \triangleq T[\mathbf{p}](I)$ are related (with slight abuse of notation) by $I(x) = \tilde{I}(T[\mathbf{p}](x))$ for all $x \in \Omega$. Equivalently, $\tilde{I}$ can be written in terms of $I$ as follows:

$$
\tilde{I}(x) = I \left( T^{-1}[\mathbf{p}](x) \right). \qquad (35)
$$

Assume $\mathbf{C}$ is a contour, i.e., a curve in 2-D or a surface in 3-D. We define the transformed contour $T[\mathbf{p}](\mathbf{C})$ to be the new contour that is obtained by applying the transformation to every point on $\mathbf{C}$. The shape represented by a contour $\mathbf{C}$ can also be represented by a binary image $I(x)$ whose value is 1 inside $\mathbf{C}$ and 0 outside $\mathbf{C}$.

*1) Registration Based on Moments:* In this section we describe the moment-based method of registration we use. We mention that this method is also described in [59] and is a rigid body transform that employs an isotropic scaling.

Let $O$ be the origin of the coordinate axes of $R^3$ and $Ox$, $Oy$, and $Oz$ be the coordinate axes. Let $C$ be a 3-D

surface in $R^3$ and $f : R^3 \longrightarrow R^3$ be a function. Then, $f(C) = \{f(x,y,z) \,|(x,y,z) \in C\}$.

The similarity transformation $T[\mathbf{p}]$ with the pose parameter $\mathbf{p} = [a\, b\, c\, \theta_x\, \theta_y\, \theta_z\, h]$ consists of translation $M(a,b,c)$, rotation $R(\theta_x,\theta_y,\theta_z)$, and scaling $H(h)$, and it maps a point $(x,y,z) \in R^3$ to $T[\mathbf{p}](x,y,z)$ as follows: $T[\mathbf{p}](x,y,z) = R(\theta_x,\theta_y,\theta_z) \circ H(h) \circ M(a,b,c) \begin{pmatrix} x \\ y \\ z \end{pmatrix} = R(\theta_x,\theta_y,\theta_z) \begin{pmatrix} h(x+a) \\ h(y+b) \\ h(z+c) \end{pmatrix}$. We describe the outline of the moments based registration scheme in Algorithm 1.

*Algorithm 1 Compute Moments Based Registration Function:* **Input:**

none $C_1$—a 3-D surface, which is a registration source $(I)$

none $C_2$—a 3-D surface, which is a registration target $\left(\tilde{I}\right)$

**Output:**

none $T[\mathbf{p}]$—a function $T[\mathbf{p}] : R^3 \rightarrow R^3$ that represents a moment-based registration scheme

**CompCanonicRegistrationFunction** $(C_1, C_2)$

1) Compute the mass centers of $C_1$ and $C_2$. Note that the mass centers are given by the vector $[m_{1,0,0}/m_{0,0,0}, m_{0,1,0}/m_{0,0,0}, m_{0,0,1}/m_{0,0,0}]$. Let $v_1$ and $v_2$ be the mass centers of $C_1$ and $C_2$, respectively.
2) Define $(a,b,c) := v_2 - v_1$, which are the parameters of the translation $M(a,b,c)$.
3) Compute the principal axes of $C_1$ and $C_2$. Let $R_1$ and $R_2$ be the $3 \times 3$ matrices that describe the directions of the inertia axes for the first and the second surface, respectively [see also (16)].
4) Let $R(\theta_x,\theta_y,\theta_z) := R_1 \cdot R_2^{-1}$.
5) Compute the volumes of $C_1$ and $C_2$. Let $m^1_{0,0,0}$ and $m^2_{0,0,0}$ be the volumes of $C_1$ and $C_2$, respectively.
6) Let $h := m^2_{0,0,0}/m^1_{0,0,0}$ which defines an isotropic scaling of $\sqrt[3]{h}$ on each one of the three axes of coordinates.

When the mass center of $\tilde{I}$ is centered in the origin, the inertia axes are parallel with the coordinate axes, and the volume of the source $I$ equals the one of $\tilde{I}$, we say that the pose of the target $\tilde{I}$ is the canonic pose of $I$. Alternatively, the mass center of $I$ together with the inertia axes defines the canonic orientation of the source.

*2) Registration Based on Energy Minimization:* In this section we describe the energy minimization based method of registration we use in 2-D for the coupled shape prior based forces. We mention that this method is also described in [39], [41].

*Alignment of Training Curves by Similarity Transforms:* We discuss how to align the $N$ training curves $\{\mathbf{C}_1, \ldots, \mathbf{C}_N\}$. In particular, a similarity transform is applied to each curve such that the transformed curves are aligned. Let us first define the similarity transform and then provide a criterion for alignment. The similarity transformation $T[\mathbf{p}]$ with the pose parameter $\mathbf{p} = [a\, b\, \theta\, h]$ consists of translation $M(a,b)$, rotation $R(\theta)$, and scaling $H(h)$, and it maps a point $(x,y) \in R^2$ to $T[\mathbf{p}](x,y)$ as follows: $T[\mathbf{p}](x,y) = R(\theta) \circ H(h) \circ M(a,b) \begin{pmatrix} x \\ y \end{pmatrix} = \begin{pmatrix} \cos(\theta) & -\sin(\theta) \\ \sin(\theta) & \cos(\theta) \end{pmatrix} \begin{pmatrix} h(x+a) \\ h(y+b) \end{pmatrix}$.

We now provide a criterion for alignment. Given $N$ training curves, we obtain aligned curves $\left\{\tilde{\mathbf{C}}_1, \ldots, \tilde{\mathbf{C}}_N\right\}$ by a similarity transformation $\tilde{\mathbf{C}}_i = T[\hat{\mathbf{p}}_i]\, \mathbf{C}_i$ with pose estimate $\hat{\mathbf{p}}_i$ for each $i \in \{1, \ldots, N\}$. The pose estimates are chosen such that they minimize an energy functional for alignment. The energy functional we use is given by

$$E_{\text{align}}(\mathbf{p}_1, \ldots, \mathbf{p}_N) = \sum_{i=1}^{N} \sum_{j=1}^{N} \left\{ \frac{\int\int_\Omega \left(T[\mathbf{p}_i] I^i - T[\mathbf{p}_j] I^j\right)^2 dxdy}{\int\int_\Omega \left(T[\mathbf{p}_i] I^i + T[\mathbf{p}_j] I^j\right)^2 dxdy} \right\} \quad (36)$$

where $I^i$ is a binary map whose value is 1 inside $\mathbf{C}_i$ and 0 outside $\mathbf{C}_i$, and $T[\mathbf{p}] I^i$ is a transformed binary map whose value is 1 inside $T[\mathbf{p}]\, \mathbf{C}_i$ and 0 outside $T[\mathbf{p}_i]\, \mathbf{C}_i$. Following (35), $I^i$ and $T[\mathbf{p}_i] I^i$ are related by $T[\mathbf{p}_i] I^i(x,y) = I^i\left(T^{-1}[\mathbf{p}](x,y)\right)$. The numerator in (36), which is the area of set symmetric difference between two interior regions of $T[\mathbf{p}_i]\, \mathbf{C}_i$ and $T[\mathbf{p}_j]\, \mathbf{C}_j$, basically measures the amount of mismatch between $T[\mathbf{p}_i] I^i$ and $T[\mathbf{p}_j] I^j$, and the denominator is present to prevent all the binary images from shrinking to improve the cost function. The double summation in (B-9) implies that we compare every pair of the binary maps in the training database. To estimate the pose parameters, we fix the pose parameter for the first curve as the one for the identity transform and compute $\mathbf{p}_2, \ldots, \mathbf{p}_N$ by

$$\{\hat{\mathbf{p}}_2, \ldots, \hat{\mathbf{p}}_N\} = \arg\min_{\hat{\mathbf{p}}_2, \ldots, \hat{\mathbf{p}}_N} E_{\text{align}}(\mathbf{p}_1, \ldots, \mathbf{p}_N) \,|\mathbf{p}_1 = [0\,0\,0\,1]$$

where we use gradient descent to compute $\mathbf{p}_2, \ldots, \mathbf{p}_N$.

*Alignment of the Candidate Curve:* Consider the problem of aligning the candidate curve $\mathbf{C}$ with the $N$ aligned training curves $\left\{\tilde{\mathbf{C}}_1, \ldots, \tilde{\mathbf{C}}_N\right\}$. To this end, we estimate a pose parameter $\hat{\mathbf{p}}$ such that $\tilde{\mathbf{C}} = T[\hat{\mathbf{p}}]\, \mathbf{C}$ is well aligned to $\left\{\tilde{\mathbf{C}}_1, \ldots, \tilde{\mathbf{C}}_N\right\}$ by minimizing an energy functional: $\hat{\mathbf{p}} = \arg\min_{\mathbf{p}} E(\mathbf{p}) = \arg\min_{\mathbf{p}} \sum_{i=1}^{N} \int_\Omega \left(T[\mathbf{p}] I - \tilde{I}^i\right)^2 dx / \int_\Omega \left(T[\mathbf{p}] I + \tilde{I}^i\right)^2 dx$ where $I$ and $\tilde{I}^i$ are binary maps whose values are 1 inside and 0 outside $\mathbf{C}$ and $\tilde{\mathbf{C}}_i$, respectively.

## ACKNOWLEDGMENT

The PD and T2 MR brain data sets were provided by the Radiology Center at Anadolu Medical Center and Yeditepe University Hospital. We would like to thank Zeynep Firat, from the Radiology Department of the Yeditepe University Hospital, for providing manual segmentation of Basal Ganglia structures for validation.

## REFERENCES

[1] A. Akselrod-Ballin, M. Galun, J. M. Gomori, A. Brandt, and R. Basri, "Prior knowledge driven multiscale segmentation of brain MRI," in *Medical Image Computing and Computer-Assisted Intervention*. New York: Springer, 2007, pp. 118–126.

[2] T. Rohlfing, D. B. Russakoff, and C. R. Maurer, Jr., "Performance-based classifier combination in atlas-based image segmentation using expectation-maximization parameter estimation," *IEEE Trans. Med. Imag.*, vol. 23, pp. 983–994, 2004.

[3] J. S. Suri, S. Singh, S. K. Setarehdan, R. Sharma, K. Bovis, D. Comaniciu, and L. Reden, "A note on future research in segmentation techniques applied to neurology, cardiology, mammography and pathology," in *Advanced Algorithmic Approaches to Medical Image Segmentation: State-of-the-Art Application in Cardiology, Neurology, Mammography and Pathology*. New York: Springer-Verlag, 2001.

[4] B. Scherrer, M. Dojat, F. Forbes, and C. Garbay, "Locus: Local cooperative unified segmentation of MRI brain scans," in *Medical Image Computing and Computer-Assisted Intervention*. New York: Springer, 2007, vol. 4791, Lecture Notes in Computer Science, pp. 219–227.

[5] J. J. Corso, Z. Tu, A. Yuille, and A. Toga, "Segmentation of subcortical structures by the graph-shifts algorithm," in *International Conference in Information Processing in Medical Imaging*. New York: Springer, 2007, vol. 4584, Lecture notes In Computer Science, pp. 183–197.

[6] K. V. Leemput, F. Maes, D. Vandermeulen, and P. Suetens, "A unifying framework for partial volume segmentation of brain MR images," *IEEE Trans. Med. Imag.*, vol. 22, no. 1, pp. 105–119, Jan. 2003.

[7] S. P. Awate, T. Tasdizen, N. Foster, and R. T. Whitaker, "Adaptive Markov modeling for mutual-information-based unsupervised MRI brain-tissue classification," *Med. Image Anal.*, vol. 10, pp. 726–739, 2006.

[8] I. William, M. Wells, W. E. L. Grimson, R. Kikinis, and F. A. Jolesz, "Adaptive segmentation of MRI data," in *Computer Vision, Virtual Reality, and Robotics in Medicine*. New York: Springer, 1995, vol. 905, Lecture Notes In Computer Science, pp. 59–69.

[9] E. Madsen and J. D. Gitlin, "Copper and iron disorders of the brain," *Annu. Rev. Neurosci.*, vol. 30, pp. 317–337, Mar. 2007.

[10] CMA, Harvard, Partial Voluming 2010 [Online]. Available: http://www.cma.mgh.harvard.edu/seg/auto_f/prob_f/partial_voluming.html

[11] J. R. Ballinger, MRI Artifacts 2009 [Online]. Available: http://www.MRItutor.org/MRItutor/artifact.htm

[12] A. Macovski, "Noise in MRI," *Magn. Reson. Med.*, vol. 36, pp. 494–497, 1996.

[13] M. Kass, A. Witkins, and D. Terzopoulos, "Snakes: Active contour models," *Int. J. Comput. Vis.*, vol. 1, no. 4, pp. 321–331, 1988.

[14] T. F. Chan and L. A. Vese, "Active contours without edges," *IEEE Trans. Image Process.*, vol. 10, no. 2, pp. 266–277, Feb. 2001.

[15] A. Tsai, A. J. Yezzi, and A. S. Willsky, "A curve evolution approach to medical image magnification via the Mumford-Shah functional," in *Medical Image Computing and Computer-Assisted Intervention*. New York: Springer, 2000, vol. 1935, Lecture Notes Comput. Sci., pp. 246–255.

[16] D. Mumford and J. M. Shah, "Boundary detection by minimizing functionals," in *Proc. 1985 IEEE Comput. Soc. Conf. Comput. Vis. Pattern Recognit.*, 1985, pp. 22–26.

[17] D. Cremers, S. J. Osher, and S. Soatto, "Kernel density estimation and intrinsic alignment for shape priors in level set segmentation," *Int. J. Comput. Vis.*, vol. 69, no. 3, pp. 335–351, 2006.

[18] J.-P. Wang, "Stochastic relaxation on partitions with connected components and its application to image segmentation," *IEEE Trans. Pattern Anal. Mach. Intell.*, vol. 20, no. 6, pp. 619–636, Jun. 1998.

[19] S. C. Zhu and A. Yuille, "Region competition: Unifying snakes, region growing, and Bayes/MDL for multiband image segmentation," *IEEE Trans. Pattern Anal. Mach. Intell.*, vol. 18, no. 9, pp. 884–900, Sep. 1996.

[20] P.-L. Bazin and D. L. Pham, "Statistical and topological atlas based brain image segmentation," *Proc. MICCAI*, vol. 1, pp. 94–101, 2007.

[21] Y. Boykov, O. Veksler, and R. Zabih, "Fast approximate energy minimization via graph cuts," *IEEE Trans. Pattern Anal. Mach. Intell.*, vol. 23, no. 11, pp. 1222–1239, Nov. 2001.

[22] Y. Cheng, "Mean shift, mode seeking, and clustering," *IEEE Trans. Pattern Anal. Mach. Intell.*, vol. 17, no. 8, pp. 790–799, Aug. 1995.

[23] J. H. Morra, Z. Tu, L. G. Apostolova, A. E. Green, A. W. Toga, and P. M. Thompson, "Automatic subcortical segmentation using a contextual model," *Proc. MICCAI*, vol. 1, pp. 194–201, 2008.

[24] V. Caselles, "Geometric models for active contours," in *IEEE Int. Conf. Image Process.*, 1995, vol. 3, pp. 9–12.

[25] G. Ho and P. Shi, "Domain partitioning level set surface for topology constrained multiobject segmentation," in *IEEE Int. Symp. Biomed. Imag.: From Nano to Macro*, 2004, vol. 2, pp. 1299–1302.

[26] J. Kim, J. W. F. , III, A. Yezzi, M.Çetin, and A. S. Willsky, "A nonparametric statistical method for image segmentation using information theory and curve evolution," *IEEE Trans. Image Process.*, vol. 14, no. 10, pp. 1486–1502, Oct. 2005.

[27] A. Yezzi, A. Tsai, and A. Willsky, "A statistical approach to snakes for bimodal and trimodal imagery," in *Proc. 7th IEEE Int. Conf. Comput. Vis.*, Sep. 1999, vol. 2, pp. 898–903.

[28] G.Ünal, A. Yezzi, and H. Krim, *Information-Theoretic Active Polygons for Unsupervised Texture Segmentation*, vol. 62, no. 3, pp. 199–220, Jun. 2005.

[29] E. Angelini, T. Song, B. Mensh, and A. F. Laine, "Brain MRI segmentation with multiphase minimal partitioning: A comparative study international," *Biomed. Imag.*, vol. 2007, no. 10526, pp. 1–15, 2007.

[30] K. Pohl, J. Fisher, S. Bouix, M. Shenton, R. McCarley, W. Grimson, R. Kikinis, and W. Wells, "Using the logarithm of odds to define a vector space on probabilistic atlases," *Med. Image Anal.*, vol. 11, no. 6, pp. 465–477, 2007.

[31] M. Rousson and N. Paragios, "Shape priors for level set representations," in *ECCV '02: Proceedings of the 7th European Conference on Computer Vision-Part II*, 2002, vol. 2351, Lecture Notes In Computer Science, pp. 78–92.

[32] Y. Chen, H. D. Tagare, S. Thiruvenkadam, F. Huang, D. Wilson, K. S. Gopinath, R. W. Briggs, and E. A. Geiser, "Using prior shapes in geometric active contours in a variational framework," *Int. J. Comput. Vis.*, vol. 50, no. 3, pp. 315–328, Dec. 2002.

[33] M. E. Leventon, W. E. L. Grimson, and O. Faugeras, "Statistical shape influence in geodesic active contours," in *Proc. 2000 IEEE Comput. Soc. Conf. Comput. Vis. Pattern Recognit.*, Jun. 2000, vol. 1, pp. 316–323.

[34] S. Dambreville, Y. Rathi, and A. Tannenbaum, "A framework for image segmentation using shape models and kernel space shape priors," *IEEE Trans. Pattern Anal. Mach. Intell.*, vol. 30, no. 8, pp. 1385–1399, Aug. 2008.

[35] Y. Chen, S. Thiruvenkadam, F. Huang, K. S. Gopinath, and R. W. Brigg, "Simultaneous segmentation and registration for functional MR images," in *Proc. 16th IEEE Int. Conf. Pattern Recognit.*, 2002, vol. 1, pp. 747–750.

[36] S. Jehan-Besson, M. Gastaud, M. Barlaud, and G. Aubert, "Region-based active contours using geometrical and statistical features for image segmentation," in *IEEE Int. Conf. Image Process.*, Sep. 2003, vol. 2, pp. 643–646.

[37] D. Cremers, C. Schnorr, and J. Weickert, "Diffusion-snakes: Combining statistical shape knowledge and image information in a variational framework," in *Proc. 1st IEEE Workshop Variational Level Set Methods in Comput. Vis.*, Washington, DC, 2001, pp. 137–144.

[38] F. Huang and J. Su, "Moment-based shape priors for geometric active contours," in *Proc. 18th IEEE Int. Conf. Pattern Recognit.*, 2006, vol. 2, pp. 56–59.

[39] A. Tsai, A. Y. , Jr, W. Wells, C. Tempany, D. Tucker, A. Fan, W. E. Grimson, and A. Willsky, "A shape-based approach to the segmentation of medical imagery using level sets," *IEEE Trans. Med. Imag.*, vol. 22, no. 2, pp. 137–154, Feb. 2003.

[40] K. Gorczowski, M. Styner, J. Y. Jeong, J. S. Marron, J. Piven, H. C. Hazlett, S. M. Pizer, and G. Gerig, "Discrimination analysis using multi-object statistics of shape and pose," in *SPIE Conf. Med. Imag.: Image Process.*, Mar. 2007, vol. 6512, pp. 1–8.

[41] J. Kim, M. Çetin, and A. S. Willsky, "Nonparametric shape priors for active contour-based image segmentation," *Signal Process.*, vol. 87, no. 12, pp. 3021–3044, Dec. 2007.

[42] B. Fischl, D. H. Salat, E. Busa, M. Albert, M. Dieterich, C. Haselgrove, A. van der Kouwe, R. Killiany, D. Kennedy, S. Klaveness, A. Montillo, N. Makris, B. Rosen, and A. M. Dale, "Whole brain segmentation: Automated labeling of neuroanatomical structures in the human brain," *Neuron*, vol. 33, pp. 341–355, Jan. 2002.

[43] A. Tsai, W. Wells, C. Tempany, E. Grimson, and A. Willsky, "Mutual information in coupled multi-shape model for medical image segmentation," *Med. Image Anal.*, vol. 8, no. 4, pp. 429–445, 2004.

[44] J. Yang, L. H. Staib, and J. S. Duncan, "Neighbor-constrained segmentation with level set based 3-D deformable models," *IEEE Trans. Med. Imag.*, vol. 23, no. 8, pp. 940–948, Aug. 2004.

[45] J. Yang and J. S. Duncan, "Joint prior models of neighboring objects for 3-D image segmentation," in *Proc. 2004 IEEE Comput. Soc. Conf. Comput. Vis. Pattern Recognit.*, 2004, vol. 1, pp. 314–319.

[46] K. Pohl, J. Fisher, R. Kikinis, W. Grimson, and W. Wells, "Shape based segmentation of anatomical structures in magnetic resonance images," in *ICCV*. New York: Springer, 2005, vol. 3765, Lecture Notes Comput. Sci., pp. 489–498.

[47] A. Litvin and W. C. Karl, "Coupled shape distribution-based segmentation of multiple objects," in *Information Processing in Medical Imaging*. New York: Springer, vol. 3565, Lecture Notes Comput. Sci., pp. 345–356.

[48] M. N. Bossa and S. Olmos, "Statistical model of similarity transformations: Building a multi-object pose model of brain structures," in *IEEE Comput. Soc. Workshop Math. Methods Biomed. Image Anal.*, New York, Jun. 2006, p. 59.

[49] C. Lu, S. M. Pizer, S. Joshi, and J.-Y. Jeong, "Statistical multi-object shape models," *Int. J. Comput. Vis.*, vol. 75, no. 3, pp. 387–404, Mar. 2007.

[50] M. Rousson and C. Xu, "A general framework for image segmentation using ordered spatial dependency," in *Medical Image Computing and Computer-Assisted Intervention*. New York: Springer, 2006, vol. 4191, Lecture Notes in Computer Science, pp. 848–855.

[51] M. Styner, K. Gorczowski, T. Fletcher, J. Y. Jeong, S. M. Pizer, and G. Gerig, "Statistics of pose and shape in multi-object complexes using principal geodesic analysis," in *International Workshop on Medical Imaging and Augmented Reality*. New York: Springer, 2006, vol. 4091, Lecture Notes in Computer Science, pp. 1–8.

[52] G. Uzunbaş, M.Çetin, G.Ünal, and A. Erçil, "Coupled nonparametric shape priors for segmentation of multiple basal ganglia structures," in *Proc. 5th IEEE Int. Symp. Biomed. Imag.: From Nano to Macro*, 2008, pp. 217–220.

[53] G. Uzunbaş, O. Soldea, M.Çetin, G.Ünal, A. Erçil, D. Unay, A. Ekin, and Z. Firat, "Volumetric segmentation of multiple basal ganglia structures using nonparametric coupled shape and inter-shape pose priors," presented at the 6th IEEE Int. Symp. Biomed. Imag. (ISBI'09), From Nano to Macro, Boston, MA, 2009.

[54] B. Fischl, D. H. Salat, A. J. van der Kouwe, N. Makris, F. Ségonne, B. T. Quinn, and A. M. Dale, "Sequence-independent segmentation of magnetic resonance images," *NeuroImage Math. Brain Imag.*, vol. 23, no. 1, pp. S69–S84, 2004.

[55] M. W. Woolrich, S. Jbabdi, B. Patenaudea, M. Chappell, S. Makni, T. Behrens, C. Beckmann, M. Jenkinson, and S. M. Smith, "Bayesian analysis of neuroimaging data in FSL," *NeuroImage*, vol. 45, no. 1, pp. S173–S186, 2009.

[56] S. M. Smith, M. Jenkinson, M. W. Woolrich, C. F. Beckmann, T. E. Behrens, H. Johansen-Berg, P. R. Bannister, M. D. Luca, I. Drobnjak, D. E. Flitney, R. K. Niazy, J. Saunders, J. Vickers, Y. Zhang, N. D. Stefano, J. M. Brady, and P. M. Matthews, "Advances in functional and structural MR image analysis and implementation as FSL," *NeuroImage*, vol. 23, no. S1, pp. S208–S219, 2004.

[57] S. J. Osher and R. P. Fedkiw, *Level Set Methods and Dynamic Implicit Surfaces*. Berlin, Germany: Springer, 2003.

[58] D. Erdogmus, R. Jenssen, Y. N. Rao, and J. C. Principe, "Gaussianization: An efficient multivariate density estimation technique for statistical signal processing," *J. VLSI Signal Process.*, vol. 45, no. 1-2, pp. 67–83, Nov. 2006.

[59] T. L. Faber and E. M. Stokely, "Orientation of 3-D structures in medical images," *IEEE Trans. Pattern Anal. Mach. Intell.*, vol. 10, no. 5, pp. 626–633, Sep. 1998.

[60] R. J. Prokop and A. P. Reeves, "A survey of moment-based techniques for unoccluded object representation and recognition," *CVGIP: Graphical Models and Image Processing*, vol. 54, no. 5, pp. 438–460, Sep. 1992.

[61] J. L. Meriam and L. G. Kraige, *Engineering Mechanics, Dynamics*, Fifth ed. New York: Willey, 2002.

[62] R. Fitzpatrick, Analytical classical dynamics course 2008 [Online]. Available: http://farside.ph.utexas.edu/teaching/336k/lectures/node80.html

[63] M. W. Spong, S. Hutchinson, and M. Vidyasagar, *Robot Modeling and Control*. New York: Willey, 2005.

[64] W. H. Press, B. P. Flannery, S. A. Teukolsky, and W. T. Vetterling, *Numerical Recipes in C: The Art of Scientific Computing*, 2nd ed. Cambridge, U.K.: Cambridge Univ. Press, 2002.

[65] R. O. Duda, P. E. Hart, and D. G. Stork, *Pattern classification*, 2nd ed. New York: Willey, 2001.

[66] L. R. Dice, "Measures of the amount of ecologic association between species," *Ecology*, vol. 26, no. 3, pp. 297–302, Jul. 1945.

[67] T. Heimann, T. Heimann, and M. Styner, Evaluation Measures 2007 [Online]. Available: http://mbi.dkfz-heidelberg.de/grand-challenge2007/sites/eval.htm

[68] M. G. Uzunbaş and O. Soldea, Ground Truth Editor 2009 [Online]. Available: http://vpa.sabanciuniv.edu/sites/medical/?file=/projects/GroundTruthEditor/index.html

[69] B. W. Silverman, *Density Estimation for Statistics and Data Analysis*. London, U.K.: Chapman Hall/CRC, 1986.

[70] The Internet Brain Segmentation Repository (IBSR) 2009 [Online]. Available: http://www.cma.mgh.harvard.edu/ibsr/

[71] Digital Imaging and Communications in Medicine NEMA, 2009 [Online]. Available: http://medical.nema.org/

[72] Analyze, Analyze and Nifti (The Neuroimaging Informatics Technology Initiative) Formats 2009 [Online]. Available: http://nifti.nimh.nih.gov/

[73] E. Cohen, R. F. Riesenfeld, and G. Elber, *Geometric Modeling With Splines: An Introduction*. Natick, MA: AK Peters, 2001.

[74] The Visualization Toolkit Kitware, 2009 [Online]. Available: http://www.vtk.org/

[75] Insight Segmentation and Registration Toolkit Kitware, 2009 [Online]. Available: http://www.itk.org/